

## Global mineral distributions on Mars

Joshua L. Bandfield

NASA Goddard Space Flight Center, Greenbelt, Maryland, USA

Received 27 April 2001; revised 29 January 2002; accepted 26 March 2002; published 27 June 2002.

[1] Determining the mineralogy of Mars is an essential part of revealing the conditions of the surface and subsurface. A deconvolution method was used to remove atmospheric components and determine surface mineralogy from Thermal Emission Spectrometer data at 1 pixel per degree (ppd). Minerals are grouped into categories on the basis of compositional and spectral similarity, and global concentration maps are produced. All binned pixels are fit well with RMS errors of  $\leq 0.005$  in emissivity. Higher RMS errors are attributed to short wavelength particle size effects on dust-covered surfaces. Significant concentrations ( $>0.10$ ) of plagioclase, high-Ca pyroxene, sheet silicates/high-Si glass, and hematite are detected and display distributions consistent with previous studies. Elevated concentrations of plagioclase and high-Ca pyroxene are consistent with basaltic surfaces and are located in low-albedo highlands regions north of  $\sim 45^\circ\text{S}$ . Significant concentrations of plagioclase and sheet silicates/high-Si glass and low concentrations of high-Ca pyroxenes are consistent with andesitic surfaces and are concentrated in both southern and northern high-latitude, low-albedo regions. Andesitic surfaces in the southern hemisphere have a lower spectral contrast than northern surfaces. An isolated surface located in Solis Planum is spectrally distinct but compositionally similar to other surfaces interpreted to be andesitic in composition. Concentrations of olivine below the detection limit correctly identify its presence in two of three locations. Potassium feldspar, low-Ca pyroxene, basaltic glass, olivine, sulfate, carbonate, quartz, and amphibole are not detected with confidence at 1 ppd. The results presented here indicate a predominance of volcanic compositions within Martian dust-free surfaces. *INDEX TERMS:* 5410 Planetology: Solid Surface Planets: Composition; 5464 Planetology: Solid Surface Planets: Remote sensing; 5470 Planetology: Solid Surface Planets: Surface materials and properties; 5494 Planetology: Solid Surface Planets: Instruments and techniques; *KEYWORDS:* Mars, infrared spectroscopy, surface mineralogy, remote sensing

### 1. Introduction

[2] An essential part of revealing the present and past conditions of the surface and the subsurface of Mars is determining its mineralogy. Igneous compositions can provide insight into mechanisms such as crustal formation, heat loss processes, and magma differentiation. Knowledge of these compositions can also be used to constrain other parameters such as bulk composition and source materials for the Martian soil and dust. Evaporite, clay, and other sedimentary compositions can provide confirmation of past liquid water environments on or near the surface. These materials may provide an idea of the temporal and spatial extent of the Martian weathering regime. Hydrothermal alteration can also produce mineral signatures that indicate a past water-rich environment. Metamorphic compositions can be used to constrain the extent to which burial and deformational mechanisms have occurred in the Martian past.

[3] The purpose of this study is to provide global distributions of Martian surface materials. The mineralogical

maps presented here allow for recovery of compositional distributions. This is distinct from previous efforts that determined surface unit distributions, which had spectral signatures defined before distributions were determined [Bandfield *et al.*, 2000a]. The compositions and distributions of materials on the surface highlight unique as well as familiar conditions and processes that have occurred during Mars' history. It is hoped that future studies will use the data set displayed here to help determine this history.

#### 1.1. Previous Spectroscopic Mineralogical Work

##### 1.1.1. Low-albedo regions

[4] Low-albedo regions on Mars (lambert albedo of less than  $\sim 0.20$  based on albedo histograms of Mellon *et al.* [2000]) have been known to contain distinct spectral absorptions near 1 and 2  $\mu\text{m}$  as well as the 10 and 20  $\mu\text{m}$  wavelength regions [Adams, 1968, 1974; Adams and McCord, 1969; Singer, 1980; Singer *et al.*, 1979; Christensen, 1982; Singer and McSween, 1993; Mustard *et al.*, 1993, 1997; Christensen, 1998]. Laboratory and telescopic and Phobos-2 Infrared Spectrometer for Mars (ISM) data have been used to determine the presence of Ca-rich pyroxenes and to conclude that olivine is not a dominant mineral phase [Singer, 1980; Singer *et al.*, 1979; McCord *et al.*, 1982;

This paper is not subject to U.S. copyright.

Published in 2002 by the American Geophysical Union.

Paper number 2001JE001510

*Mustard et al.*, 1993]. *Mustard et al.* [1997] investigated the  $\sim 1 \mu\text{m}$  and the  $\sim 2.2 \mu\text{m}$  absorptions in ISM data and argued for the coexistence of variable relative abundances of both low-Ca and high-Ca pyroxenes within several equatorial dark regions. The presence of these pyroxenes is consistent with the compositions of a variety of igneous compositions, including the olivine-poor SNC meteorites, basalts, andesites, and komatiites.

[5] Distinct absorptions in the 9 and 20  $\mu\text{m}$  spectral regions were observed in Viking Infrared Thermal Mapper (IRTM) data [*Christensen*, 1982, 1998]. The shape and depth of the absorptions correlate well with dark regions and are consistent with basalt-like sand surfaces. However, the coarse spectral resolution makes unique compositional determination impossible and atmospheric removal difficult [*Christensen*, 1998].

### 1.1.2. High-albedo regions

[6] A great deal of past spectroscopic work has focused on the composition of Martian high-albedo regions (lambert albedo of greater than  $\sim 0.20$  based on albedo histograms of *Mellon et al.* [2000]). Investigations in the visible and near-infrared (VNIR) portions of the spectrum have been extensive with respect to Martian high-albedo, low thermal inertia (and presumably dusty) surfaces (see review by *Bell* [1996]) [*Bell et al.*, 2000; *Morris et al.*, 2000]. While the details of this work are considerable, these surfaces may be partially characterized by poorly crystalline iron oxides. In addition, minor absorptions in the spectral shape strongly suggest a small amount of crystalline iron oxide ( $\sim 2\text{--}4 \text{ wt}\%$ ) [*Bell et al.*, 1990; *Morris et al.*, 1997].

[7] The high-albedo regions of Mars display subtle spectral differences as seen by Viking and Phobos-2 orbiter, Pathfinder lander, and telescopic observations [*Soderblom et al.*, 1978; *McCord et al.*, 1982; *Murchie et al.*, 1993; *Geissler et al.*, 1993; *Merenyi et al.*, 1996; *Bell and Morris*, 1999; *Bell et al.*, 2000; *Morris et al.*, 2000]. These results indicate spatial variations in the abundance and, possibly, the composition of well-crystallized iron oxide materials. Spectral detection of sulfate and other evaporite materials in the Martian soil and dust remains elusive despite abundant chemical evidence for oxidized sulfur [*Toulmin et al.*, 1977; *Clark et al.*, 1982; *Morris et al.*, 2000] as well as evidence for duricrust material at the Viking and Pathfinder landing sites and from Mars Global Surveyor (MGS) Mars Orbiter Camera (MOC) images [*Malin et al.*, 1998].

### 1.1.3. Atmospheric dust

[8] A number of studies have investigated the Martian atmospheric dust in thermal infrared wavelengths using both the Mariner 9 Infrared Interferometric Spectrometer (IRIS) and the IRTM instruments [e.g., *Conrath et al.*, 1973; *Toon et al.*, 1977; *Martin and Richardson*, 1993]. The  $\sim 8\text{--}12 \mu\text{m}$  and  $\sim 20\text{--}50 \mu\text{m}$  wavelength regions contain prominent atmospheric dust absorptions coincident with those of a number of materials, including silicates, oxides, and sulfates. In order to perform compositional studies a number of physical effects that influence the absorption shape need to be accounted for, especially particle-size distribution and single-scattering albedo. These effects prohibit direct analysis of the measured spectra. Analyses of the Martian atmospheric dust have historically focused on the forward problem: using optical constants of various materials to simulate the measured Martian spectrum [*Hunt*

*et al.*, 1973; *Aronson and Emslie*, 1975; *Toon et al.*, 1977; *Clancy et al.*, 1995]. While the results have demonstrated that the Martian dust may be composed of materials similar to montmorillonite and palagonite, there are clear discrepancies between the Martian spectra and those approximated using the optical constants of these materials.

## 1.2. Previous Thermal Emission Spectrometer Results

[9] The Thermal Emission Spectrometer (TES) on board the MGS spacecraft has returned data in the  $200\text{--}1650 \text{ cm}^{-1}$  ( $\sim 6\text{--}50 \mu\text{m}$ ) portion of the spectrum (see a brief instrument description below as well as thorough descriptions of the TES instrument and operations by *Christensen et al.* [1992] and *Christensen et al.* [2001a]). A number of studies have been used to determine the spectral properties and composition of the surface of Mars.

[10] TES aerobraking data from the Sinus Meridiani region of Mars contain prominent absorptions at  $\sim 300$ , 450, and  $>525 \text{ cm}^{-1}$ , which closely match the absorptions of coarse-grained, gray hematite [*Christensen et al.*, 2000a]. Subsequent investigation of the global data set discovered additional concentrations of hematite within Aram Chaos and within the Ophir/Candor regions of Valles Marineris [*Christensen et al.*, 2001b]. Spectroscopic evidence indicates that these materials were most likely formed from precipitation from aqueous fluids, and morphologic features such as layered, friable units of these localities suggest a sedimentary environment [*Christensen et al.*, 2000a, 2001b]. The hematite is distinct from the nanophase and red hematite detected in high-albedo regions that form under weathering and alteration processes.

[11] Inspection of atmospherically corrected [*Bandfield et al.*, 2000b; *Smith et al.*, 2000] TES data reveals distinct  $\sim 400$  and  $1000 \text{ cm}^{-1}$  absorptions in low-albedo regions, consistent with earlier studies [*Christensen*, 1982]. An initial study of atmospherically corrected spectra acquired of Cimmeria Terra revealed a surface composed primarily of plagioclase feldspar and high-Ca pyroxene that closely matches the spectral signature of typical terrestrial basaltic sands [*Christensen et al.*, 2000b]. Global mapping revealed two major distinct spectral units within Martian low-albedo regions [*Bandfield et al.*, 2000a]. Average spectra of these two spectral units were isolated and, using both direct comparison with terrestrial samples and deconvolution techniques, were found to match basaltic and andesitic compositions. The basaltic mineralogy was found to be similar to that of *Christensen et al.* [2000b], and the andesitic unit was dominated by plagioclase feldspar and high-Si glass. The andesitic units are most concentrated in the northern lowland regions, while the basaltic compositions are restricted to low-albedo regions in the southern highlands.

[12] High-albedo regions have very little absorption in the  $\sim 400$  and  $1000 \text{ cm}^{-1}$  spectral regions [*Christensen*, 1982; *Bandfield et al.*, 2000b; *Bandfield and Smith*, 2001]. However, deep absorptions are present at short wavelengths outside of the wavelength regions covered by initial atmospheric correction methods [*Bandfield and Smith*, 2001]. This spectral signature is consistent with materials such as fine-grained silicates present on the surface. The deep short-wavelength absorption is correlated with low thermal inertia values, which are indicative of fine-grained particulates

[Ruff *et al.*, 2001]. The behavior of fine-grained particulate surfaces in the thermal infrared is not well understood, and compositions are difficult to confirm.

### 1.3. Goal of This Study

[13] This study extends upon the previous TES investigations and provides a global data set of surface mineralogy as determined by the TES instrument. The previous investigations discussed above have revealed many of the details of the TES data set and the methods used to interpret it. The data set and methods have been demonstrated to be consistent and robust, allowing for the transition from producing surface unit maps to global maps of individual minerals. In addition to investigating global surface compositions and mineralogies, the global mineral maps presented here may be used to discover locally or regionally distinct surface compositions that are not otherwise easily located.

## 2. Approach

### 2.1. TES Instrument and Data Set Overview

[14] The TES instrument is a Fourier Transform Michelson Interferometer that covers the wavelength range from 1700 to 200  $\text{cm}^{-1}$  ( $\sim 6$  to 50  $\mu\text{m}$ ) at 10 or 5  $\text{cm}^{-1}$  sampling [Christensen *et al.*, 1992]. The instrument also contains bore-sighted thermal (5–100  $\mu\text{m}$ ) and visible/near-infrared (0.3–3.5  $\mu\text{m}$ ) bolometers. The focal planes in each wavelength consist of three cross-track and two along-track detectors with an instantaneous field of view of  $\sim 8.5$  mrad. The TES instrument uses a pointing mirror that allows for limited targeting capability, limb observations, image motion compensation (IMC), emission phase function measurements, and periodic calibration by observing space and an internal reference surface. The final 2 hour,  $\sim 380$  km altitude mapping orbit provides a surface sampling of  $3 \times \sim 8$  km. The elongated pixel dimension is due to the final mapping orbit of MGS, which begins its orbit at 0200 local time (LT) rather than the intended 1400 LT because of damage to the solar panel that required lower aerobraking rates. Spacecraft direction relative to the surface is reversed, and IMC does not produce adequate results when stepping the mirror in the direction opposite that originally intended. As a result, spatial sampling is smeared in the along-track direction. For a complete description of the instrument as built and instrument operations, see Christensen *et al.* [2001a].

[15] A linear response function for each of the six detectors is derived periodically from observations of space and an internal reference surface of known emissivity and temperature. Three scans each of space and the reference surface are taken and averaged for each detector. The linear response function allows for a simple conversion from raw spectra into calibrated radiance. All spectra used in this study were converted into apparent emissivity by dividing out a Planck curve of the highest brightness temperature within a band of 50  $\text{cm}^{-1}$ . This brightness temperature is also assumed to be the surface temperature. For a complete description of radiometric calibration, see Christensen *et al.* [2001a].

[16] The data used in this study were from the mapping orbit data set up to orbit 5317 (ock 7000,  $L_s$  104°–352°). The orbit range was restricted due to an instrument anomaly that grew progressively worse past this period. This anomaly causes a sporadic minor feature to appear in spectral data at

$\sim 1000 \text{ cm}^{-1}$ . The cause of this anomaly is unclear at this time, though it is similar to other features that are correlated with spacecraft vibrations. Data were limited to spectra of surface temperatures  $>250$  K, dust extinctions of  $<0.18$  (1075  $\text{cm}^{-1}$  opacity of  $\sim 0.3$ ), water ice extinctions of  $<0.1$  (800  $\text{cm}^{-1}$  opacity of  $\sim 0.15$ ), and emission angles of  $<30^\circ$ . In addition, a number of quality parameters in the TES database were used to restrict anomalous data such as spectra containing phase inversions due to lost bits. Only 10  $\text{cm}^{-1}$  data were used for this study, which represents  $>99\%$  of the data collected for the orbit range used.

[17] The emissivity spectra were binned and averaged into a global map of 1 pixel per degree. This was done for two reasons: (1) Averaged spectral data contain a lower random and systematic noise level. (2) Processing time required to deconvolve the TES spectra is reduced by up to several orders of magnitude from about a year to several hours. Some concern may be raised in averaging spectra from two contrasting atmospheric conditions such as a spectrum measured during a dust storm and a spectrum measured over the aphelion water ice cloud belt. However, data were restricted to prevent such extreme atmospheric conditions, and atmospheric components have been demonstrated to combine in an extremely linear manner [Bandfield *et al.*, 2000b]. As high resolutions are not necessary for this initial global study, only 1 pixel per degree maps are discussed in this paper.

### 2.2. Algorithm Description

[18] It has been demonstrated that the thermal infrared spectrum of a mixed surface may be closely modeled using a linear combination of the end-member spectra weighted by the aerial concentration of each end-member [Gillespie, 1992; Thomson and Salisbury, 1993; Ramsey and Christensen, 1998; Ramsey *et al.*, 1999; Ramsey and Fink, 1999; Feely and Christensen, 1999; Hamilton and Christensen, 2000]. The deconvolution provides a linear least squares fit of the measured spectra using combinations of the end-member spectra, and the weightings represent the component areal abundances [Ramsey and Christensen, 1998].

[19] The linear model may be extended to the surface atmosphere interaction in the thermal infrared for Mars. Atmospheric correction and mineral abundance determination are performed simultaneously using the Deconvolution Method described by Bandfield *et al.* [2000b], Christensen *et al.* [2000b], and Smith *et al.* [2000]. This method assumes that each TES apparent emissivity spectrum may be modeled as a linear combination of both surface and atmospheric end-members [Bandfield *et al.*, 2000a, 2000b; Smith *et al.*, 2000]. The resulting concentrations of the surface component end-members may be normalized to retrieve their areal concentrations and the atmospheric concentrations represent extinctions that may be used with the retrieved temperature profile from the 667  $\text{cm}^{-1}$   $\text{CO}_2$  band [Conrath *et al.*, 2000] to retrieve atmospheric opacities.

[20] The least squares fit algorithm used here is similar to that described by Ramsey and Christensen [1998]. The routine is an iterative program that successively removes surface component concentrations that are less than zero and therefore unrealistic. This iterative process may find only a local, rather than global, minimum. Although this raises the possibility of inaccuracies, Feely and Christensen

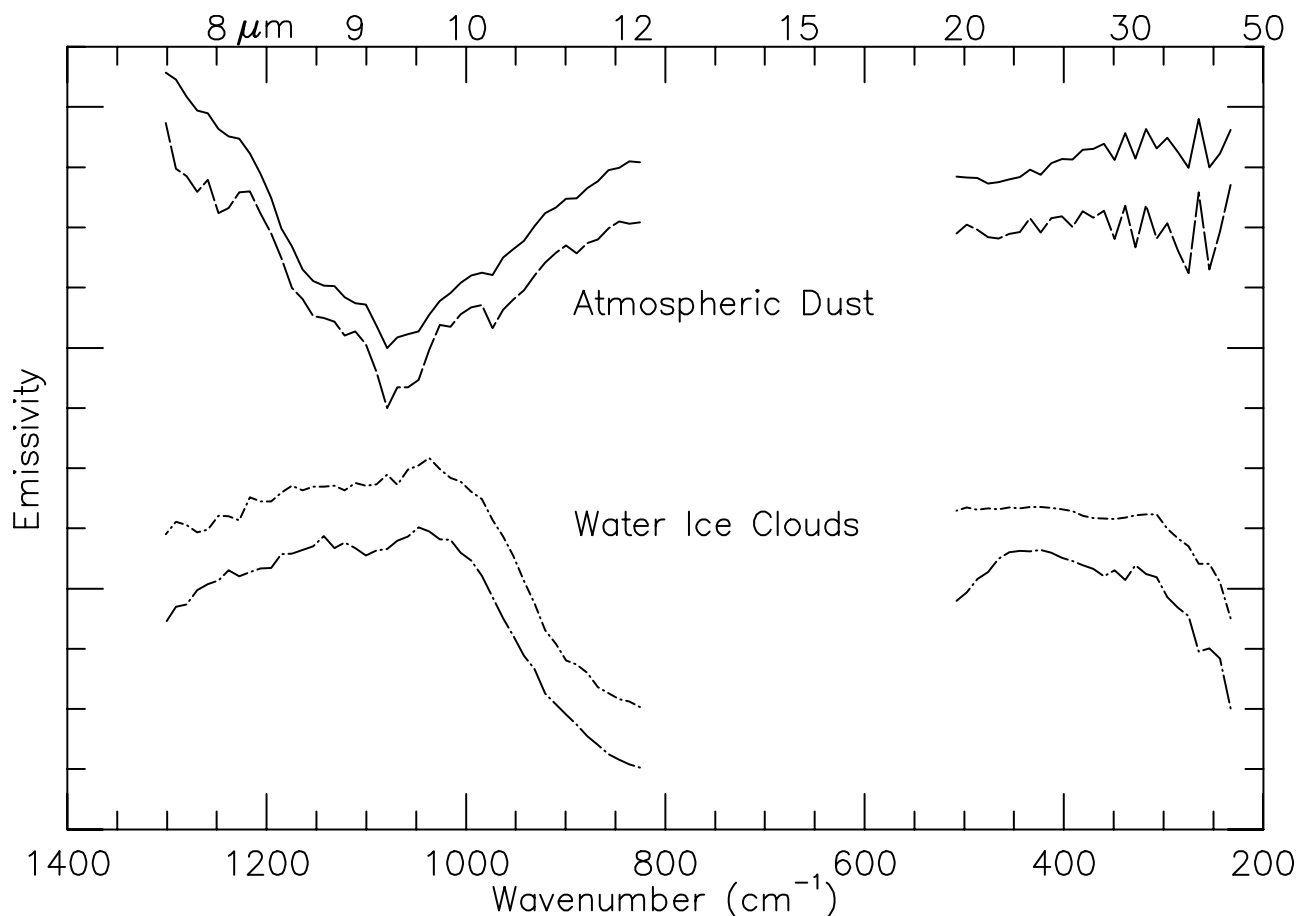


**Figure 1.** Atmospheric particulate spectral shapes used for fitting the TES spectra (offset for clarity). Differences in atmospheric dust shapes are due to relative contribution of  $\text{CO}_2$  and water vapor minor absorptions resulting from variations in atmospheric dust loading. Primary differences in water ice spectral shape are at  $\sim 500 \text{ cm}^{-1}$  due to variations in particle size.

[1999] and *Hamilton and Christensen* [2000] have applied this method extensively and found no adverse or systematic defects due to the iterative process. Spectra were fit to the TES  $10 \text{ cm}^{-1}$  spectral channels 9–35 and 65–110, corresponding to  $233\text{--}508 \text{ cm}^{-1}$  and  $825\text{--}1301 \text{ cm}^{-1}$ , respectively. The extreme low and high wave number portions of the spectrum were cut out because they contain higher random and systematic noise levels and are marked by nearly continuous water vapor and  $\text{CO}_2$  absorptions. The  $508\text{--}825 \text{ cm}^{-1}$  spectral region was cut to remove the  $667 \text{ cm}^{-1}$   $\text{CO}_2$  absorption, which contains numerous sharp absorptions with opacities  $\gg 1$ .

[21] Atmospheric dust and water ice spectral end-members were isolated using the target transformation and end-member recovery techniques as described by *Bandfield et al.* [2000b]. About 10 spectral shapes each of both atmospheric water ice and dust were isolated from individual data subsets. These atmospheric shapes could be categorized into two groups each for water ice and dust, and the retrieved spectra in each category was averaged to obtain the end-members used for this analysis (Figure 1). The dust end-members represent periods of high and low opacity [*Bandfield et al.*, 2000b], and the two water ice end-members represent small and large particle size distributions that have been observed in the TES data set [*Clancy et al.*,

2000]. Negative concentrations are allowed in the algorithm for the atmospheric end-members to allow for conditions outside of the range that is covered by the end-members. For example, if a period of data collection is characterized by lower dust opacities than represented between the two atmospheric dust end-members, the algorithm may extrapolate to this condition by using negative concentrations of the high-opacity atmospheric dust end-member and positive concentrations of the low atmospheric dust end-member. Negative concentrations of both end-members were never required to fit the TES spectra, and physical reality was not violated by the model. Though the atmospheric dust end-members contain minor  $\text{CO}_2$  and water vapor absorption bands, an additional synthetic water vapor [*Smith*, 2002] and a synthetic  $\text{CO}_2$  spectrum (similar to *Maguire* [1977]) formulated for the Martian atmosphere were added to better cover the range of conditions covered by the TES instrument at Mars [see *Smith et al.*, 2001]. This allows for better coverage of the variable intensities of dust, water vapor, and  $\text{CO}_2$  signatures, which can be independent and not completely modeled using only two spectral shapes.

### 2.3. End-Member Set

[22] Mineral end-members were selected to cover a broad range of compositions (Table 1), and the majority was

**Table 1.** End-Members Used for Deconvolution of TES Emissivity Data Sets<sup>a</sup>

End-Member Category	Name	ASU Library Number	
Quartz	quartz	136	
Potassium feldspar	microcline	95	
Plagioclase	albite	4	
	oligoclase	15	
	andesine	79	
	labradorite	10	
	bytownite	76	
	anorthite	123	
	actinolite	26	
Amphibole	actinolite	26	
Low-Ca pyroxene	enstatite	51	
	bronzite	58	
High-Ca pyroxene	diopside	69	
	augite	57	
	augite	134	
	hedenbergite	59	
Olivine	forsterite	5	
	fayalite	167	
Sheet silicate/high-Si glass	Si-K glass	–	
	biotite	80	
	muscovite	17	
	chlorite	9	
	serpentine	24	
	serpentine	34	
	nontronite	151	
	Fe-smectite	157	
	illite	93	
	Low-Si glass	basaltic glass	–
	Oxide	hematite	30
Sulfate	anhydrite	103	
	gypsum	100	
Carbonate	calcite	114	
	dolomite	142	
	–	–	
Atmosphere	low-opacity dust	–	
	high-opacity dust	–	
	water ice (small)	–	
	water ice (large)	–	
	Synth. CO <sub>2</sub>	–	
	Synth. Water Vapor	–	

<sup>a</sup>TES, Thermal Emission Spectrometer; ASU, Arizona State University.

selected from the Arizona State University spectral library [Christensen *et al.*, 2000c]. Two glass spectra were included: a high-Si potassium glass similar to obsidian and a quenched basaltic glass. Both of these samples are described by Wyatt *et al.* [2001]. Although it is desirable to include many compositions to avoid making a priori assumptions, it is also necessary to limit the number of end-members to keep the least squares fit solution as stable as possible. When the number of linearly independent spectral end-members equals the number of spectral channels, the system is determined and the fit will be perfect regardless of the end-member set and the spectrum being fit. However, unless the number of end-members approaches the number of spectral channels, it is extremely unlikely for the algorithm to fit a spectrum with an arbitrary set of mineral spectra unrelated to those actually present. To balance these two opposing conditions, 32 minerals and glasses were selected in addition to 6 atmospheric end-members and a blackbody to fit the 73 spectral channels of TES data used in this analysis. End-members were selected to emphasize igneous and sedimentary compositions.

[23] Several minerals were intentionally not included in the end-member set. Many metamorphic compositions, such as kyanite, garnet, and wollastonite, are not included in the end-member set as there is little evidence for the presence of

these minerals on the Martian surface. Only one amphibole, an actinolite, was included in the end-member set. High concentrations of amphiboles have not been widely expected on the surface, nor has there been much indication of amphiboles from spectral and other data sets. Actinolite does not cover the variety of amphiboles by any measure, but the variety was limited to constrain the total number of end-members. Though actinolite, a metamorphic mineral, may not necessarily be the most likely amphibole present, its spectral signature is similar to its related minerals. As presented below, there is no sign of the presence of actinolite, and as a result, there is little evidence for amphiboles in general.

[24] An additional end-member not included was pigeonite, which has been widely expected to exist on the Martian surface in high abundances. A synthetic pigeonite sample has been used by Wyatt *et al.* [2001]; however, the quality of the sample for use as a coarse particulate spectral standard is marginal. For this study it was decided not to include this sample, as its inclusion in previous attempts to deconvolve TES spectra has not significantly changed the results of this analysis or the quality of spectral fitting. Previous studies have noted that Martian meteorite samples with high amounts of pigeonite are not consistent with TES surface spectra [Christensen *et al.*, 2000b; Hamilton *et al.*, 2001a].

## 2.4. Output Data Sets

[25] The deconvolution algorithm produces several output data sets: end-member concentrations, modeled TES spectra, atmosphere-removed TES spectra, and modeled surface spectra. These are all in image cube form with 73 channels for the spectral output data sets and 40 channels for the concentrations (39 end-members plus RMS error). Output concentrations are primarily viewed spatially, while the other data sets are primarily used for spectral analysis.

[26] With the number of spectra numbering tens of millions, it is necessary to use methods such as those presented here to coherently investigate the entire data set. The purpose of the mineral concentration maps is to locate new spectral features in addition to providing spatial distributions of known spectral attributes. Spectrally unique regions may be indicated by either the RMS error image or the mineral concentration images. The RMS error image can indicate regions where spectral features are not matched well by the end-member spectra used to fit the measured TES spectra. Other factors, such as surface temperature and atmospheric effects may also greatly influence the RMS error, however. Mineral abundance images may also be used to locate mineralogically unique regions on the surface. This may be the case even when mineral concentrations are below detection limits. The mineral itself may not be confidently identified; however, if a spatially coherent pattern is present, there is some indication that the region is spectrally unique and may be investigated more closely.

[27] Minerals are reported throughout this paper as concentrations: the signal strength relative to the mineral end-member used in the deconvolution. The concentration can be affected by both the areal coverage of the individual minerals present as well as the surface texture, which affects spectral contrast. This is the most appropriate number to use for searching for and detecting the signature of a specific mineral because the number is not modified by additional

assumptions. Where rock types are discussed, it is more appropriate to use normalized mineral percentages to obtain relative mineral abundances.

## 2.5. Uncertainties

[28] The combined random and systematic error in emissivity as determined by *Christensen et al.* [2000b] for an average of six detectors and a surface temperature of 280 K is  $<0.0013$  from 300 to  $1100\text{ cm}^{-1}$  and increasing to 0.0035 at  $1400\text{ cm}^{-1}$ . Most of the 1 degree binned TES spectra included larger numbers of spectra in their averages as well as multiple orbits that significantly reduce the systematic noise introduced with calibration. As a result, the errors in measured emissivity may be significantly lower. As discussed above and by *Bandfield et al.* [2000a], standard deviations in the surface spectral shape acquired of similar surfaces under clear atmospheric conditions are low (commonly 0.002 in emissivity or less).

[29] Systematic error due to atmospheric removal and the least squares fitting methods is also a significant source of uncertainty in Martian surface compositional analysis with TES. Two separate atmospheric correction methods were independently developed and applied to TES spectra of the same basaltic surface, each under widely different atmospheric conditions, to assess their uncertainties [*Smith et al.*, 2000; *Christensen et al.*, 2000b]. Standard deviations are low throughout the spectral range used in this analysis, commonly at  $\sim 0.002$  in emissivity. Both atmospheric correction methods have been applied to surfaces of other compositions with similar results.

[30] *Christensen et al.* [2000b] used deconvolution results as well as visual analysis of synthetic spectral models to determine a mineral abundance accuracy and detection threshold of 10–15%. These abundances are after being normalized for blackbody used in the deconvolution, which is at concentrations of 40–50%, consistent with sand-sized particulates. Since mineral concentrations reported here are absolute and not normalized for blackbody as previously reported abundances were, the accuracy and detection threshold has been determined before normalization and is correspondingly lower at  $\sim 0.05$ – $0.10$  (5–10%). Surface temperatures used in this analysis range from 250 to 310 K but are generally lower than the  $\sim 280$  K used by *Christensen et al.* [2000b]. Despite greater numbers of spectra used for averaging, lower surface temperatures as well as the use of generic atmospheric spectral shapes suggest that the upper limit (0.10) error should be used for the mineral maps presented here.

[31] Several other methods may be used to determine uncertainties in this analysis. Several mineral groups, such as oxides and carbonates, have spectral signatures with distinctive and sharp absorptions. When these materials are mixed in surfaces with a much lower degree of modulation within the wavelength regions of these sharp bands, their detectability by visual analysis and band matching techniques is greatly enhanced. Several minerals investigated by these methods with the TES data may be used as an independent method to establish the error and detection limits of the mineral maps presented here.

[32] Hematite was detected by the TES instrument on the basis of narrow and deep absorptions present at low wave numbers and even apparent in spectra with no atmospheric

removal [*Christensen et al.*, 2000c]. Band indices and careful visual analysis have inspected the TES data set for surface exposures of hematite with an error of  $\sim 0.02$  [*Christensen et al.*, 2001b]. These studies found no significant occurrences of hematite outside of Sinus Meridiani, Valles Marineris, and Aram Chaos. As the Valles Marineris hematite exposures were at the limit of TES resolution, they are not expected to be observed in 1 pixel per degree binned maps. The hematite mineral map, which will be discussed in detail below, does indicate that concentrations of 0.10–0.20 are present in the Aram Chaos and Sinus Meridiani locations. The maps also display concentrations elsewhere of 0–0.10 in regions that *Christensen et al.* [2001b] found to contain concentrations of  $<0.02$  hematite.

[33] Carbonate spectra contain prominent absorptions near 350, 890, and  $1500\text{ cm}^{-1}$ . The  $1500\text{ cm}^{-1}$  absorption is distinctive enough with respect to silicates to be easily detected visually. The lack of significant absorption in moderate- to low-albedo regions at  $1500\text{ cm}^{-1}$  in TES spectra with minor  $\text{CO}_2$  and water vapor absorptions removed may be used to limit carbonate concentrations to significantly less than 0.10 [*Bandfield and Smith*, 2001; *Christensen et al.*, 2001a]. The carbonate mineral map (discussed in more detail below) commonly displays concentrations of  $\sim 0.05$ – $0.07$  and up to  $\sim 0.09$  in the same regions where carbonate concentrations were limited by the previous studies. This feature is outside the spectral range covered by the algorithms presented here but is clearly not present within a spectrally flat continuum in surface spectra recovered by *Bandfield and Smith* [2001]. Visual inspection of the uncorrected TES spectra used in this study also did not display significant absorptions at these wavelengths within regions with relatively high concentrations recovered by the algorithm.

[34] The comparisons of the results presented here and previous studies of oxides and carbonates agree well with the 0.10 uncertainty and detection limit stated above. Strictly, errors are in fact different for each mineral and dependent on the concentrations of each other material present. These errors, however, are impossible to determine without first knowing the mineralogy. Analyses of deconvolution studies have found this error to be consistent in practice and not highly dependent on end-member mineral groups and unknown samples [*Ramsey and Christensen*, 1998; *Feely and Christensen*, 1999; *Hamilton and Christensen*, 2000]. Some dependence of error with individual end-member groups is expected, however, and *Wyatt et al.* [2001] found small systematic deconvolution errors within individual mineral groups for laboratory spectra from a range of mafic to intermediate volcanic compositions.

## 3. Results

### 3.1. Mineral Distributions

[35] Each of the mineral maps was placed into one of 11 categories (Table 1) and summed to produce a map for each mineral category. Selection of minerals for each category was based on spectral and compositional similarity. This was done to reduce error and increase confidence in the compositional maps, as it is easier to distinguish between a carbonate and a sulfate than it is to distinguish a calcite from

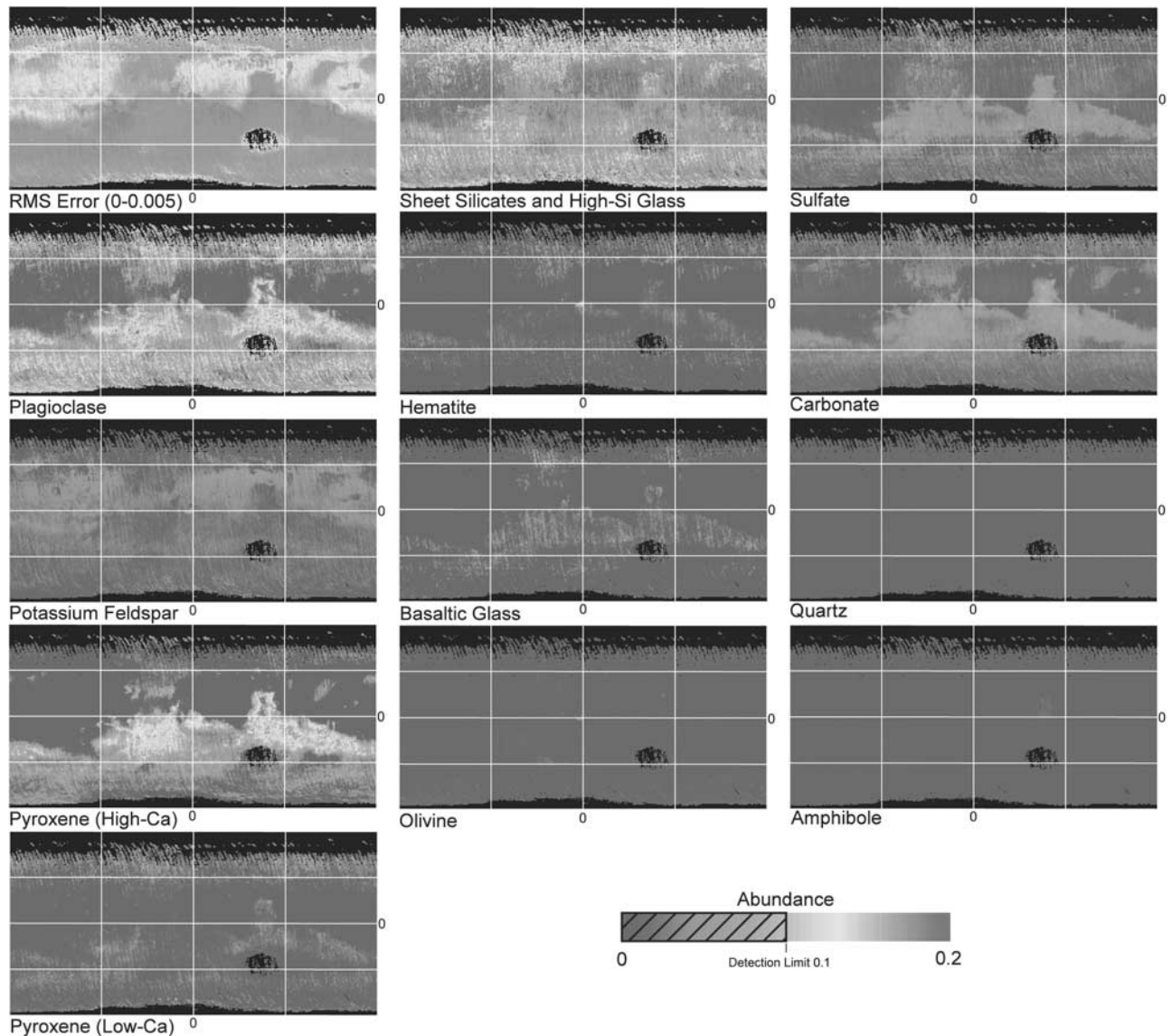


**Figure 2.** One pixel per degree binned global mineral concentration maps. The scale ranges from blue (concentration = 0) to red (concentration  $\geq 0.2$ ) except the RMS error image, which is 0 to 0.005 in emissivity from blue to red, respectively. Colors that are below the detection limit are hatched on the scale bar. The concentrations represent weightings relative to the mineral end-members used in the deconvolution (see text). Mineral groupings are described in the text and are listed in Table 1. See color version of this figure at back of this issue.

a dolomite, for example. Each of the 11 categories contains spectral end-members that have clear, distinguishing features from the end-members in other categories. In most cases the spectral similarities are related to compositional similarities with the exception of high-Si glass and sheet silicates. It is difficult to confidently distinguish these two classes using deconvolution alone with general atmospheric end-members on binned orbital data from a variety of surface temperatures and atmospheric conditions. High-Si glass has been consistently identified and distinguished from sheet silicates using individually retrieved atmospheric end-members to recover surface spectral signatures under optimal conditions from a variety of high spectral contrast locations within individual orbits [Bandfield *et al.*, 2000b]. All mineral concentration images were limited to areas with

RMS errors between measured and modeled spectra of  $<0.005$ .

### 3.1.1. RMS error

[36] With several exceptions, all spectra were fit well with RMS error between measured and modeled spectra of less than  $\sim 0.0045$  in emissivity (Figures 2a and 3). Much higher errors are encountered in  $\ll 1\%$  of the data near the extremes of coverage, including near the edges of the permanent polar caps and Hellas basin that are characterized by either cold and icy or warm and dusty atmospheric conditions. Dark regions and southern highlands regions produced lower RMS errors (less than  $\sim 0.0015$ ) than northern hemisphere light regions. There are several distinguishing areas of relatively high error outside of the fringe regions such as Arabia Terra to the northwest of Syrtis Major and to the northeast of Elysium.

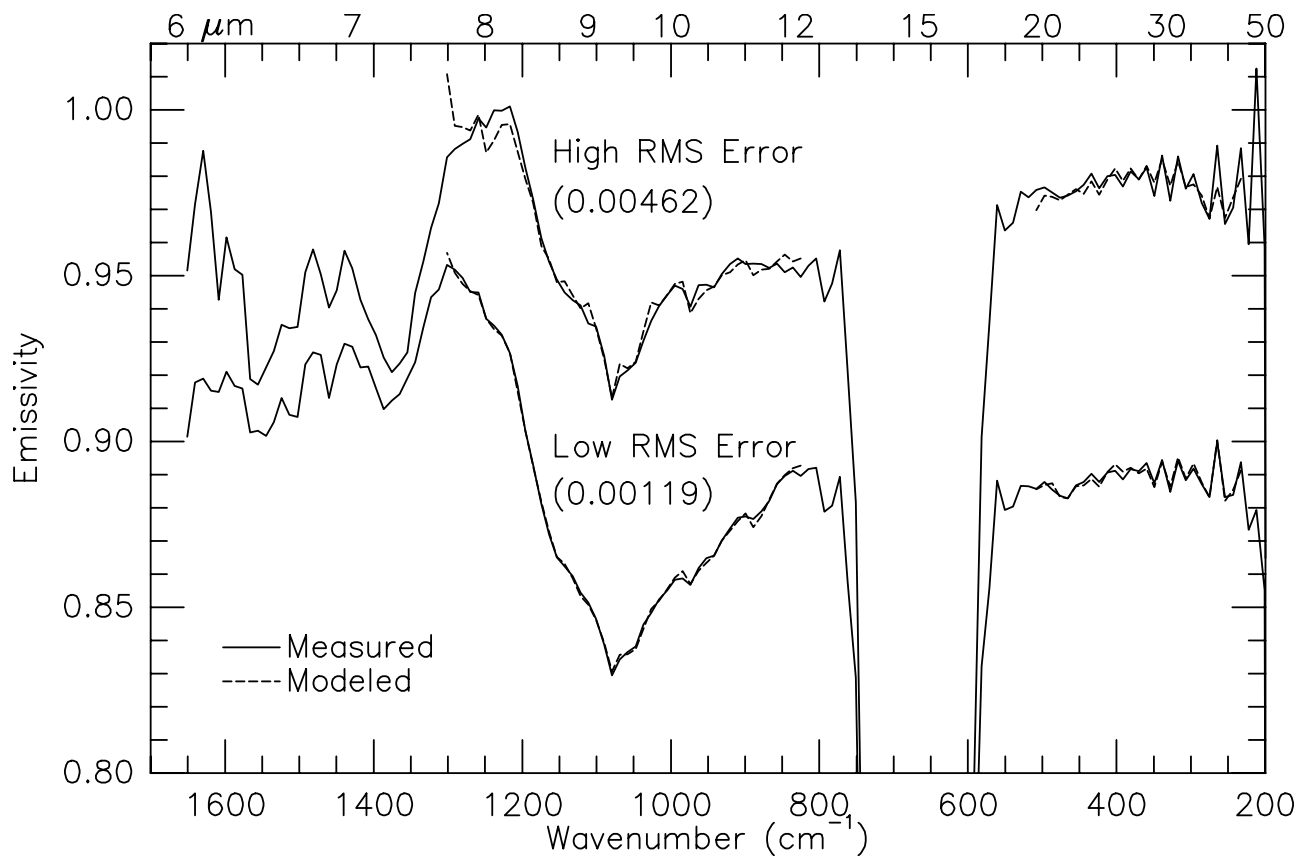


**Figure 3.** Measured (solid) and modeled (dashed) TES spectra (offset by 0.05 for clarity) displaying the range of quality of fit. Though in both cases most features are modeled, the small deviations in the high RMS error spectrum (located in a dusty, high-albedo region) indicate that the correct surface end-members are not included in the least squares fitting algorithm.

Both of these regions are high-albedo surfaces and have RMS errors between measured and modeled spectra of  $\sim 0.0035$ – $0.0045$ .

### 3.1.2. Feldspars

[37] Feldspars were separated into two categories: potassium feldspar and plagioclase. The potassium feldspar image displays no areas with concentrations greater than  $\sim 0.07$  (Figure 2a). The northern hemisphere high-albedo regions display concentrations commonly  $\sim 0.05$ , and concentrations are much lower outside of these regions. No potassium feldspars are present at or above the limit of detection (0.10). Plagioclase is present in high concentrations in low-albedo regions. High-latitude, low-albedo regions have concentrations of  $\sim 0.05$ – $0.15$ . Equatorial low-albedo regions display concentrations of  $\sim 0.10$ – $0.20$  with the highest concentrations in the Syrtis Major region. High-albedo surfaces have plagioclase concentrations of  $0$ – $0.05$ , well below the detectable limit. Where there are significant concentrations, average plagioclase compositions are intermediate to calcic.

### 3.1.3. Pyroxenes

[38] Pyroxenes were also separated into two categories: high calcium and low calcium. High-Ca pyroxenes are identified in concentrations of  $0.10$ – $0.20$  in equatorial low-albedo regions (Figure 2a). Again, the highest concentrations are present in Syrtis Major. High-latitude, low-albedo regions are characterized by concentrations of  $0$ – $0.10$ . Light regions

have  $0$ – $0.05$  high-Ca pyroxene concentrations. Only equatorial low-albedo regions have pyroxene concentrations above the detection limit.

[39] Low-calcium pyroxenes have primarily low concentrations ( $0$ – $0.05$ ) over the entire planet with the exception of some regions with slightly higher concentrations in northern hemisphere, low-albedo regions ( $0.05$ – $0.10$ ; Figure 2a). In all cases, low-Ca pyroxenes remain under the detection limit.

### 3.1.4. Sheet silicates and high-Si glass

[40] The sheet silicate and high-Si glass image is slightly noisier than the other maps (Figure 2a). This is likely due to the spectral similarity between the sheet silicate and high-Si glass end-member group and the atmospheric dust spectral shapes. The highest concentrations are located in northern hemisphere low-albedo regions with concentrations of  $0.05$ – $0.20$ . High concentrations are also present in several isolated regions south of Solis Planum, southeast of Hellas Basin, and along the edge of the southern polar cap. High-albedo regions contain  $0$ – $0.10$  sheet silicate and high-Si glass concentrations. Equatorial and southern hemisphere low-albedo regions have concentrations of  $0.05$ – $0.15$  with the exception of the isolated areas mentioned.

### 3.1.5. Hematite

[41] Hematite is identified above the detection limit in only two locations: Sinus Meridiani ( $0.10$ – $0.20$ ) and a single pixel within Aram Chaos ( $0.10$ – $0.15$ ). Most other locations have concentrations of  $0$ – $0.05$  with the exception of

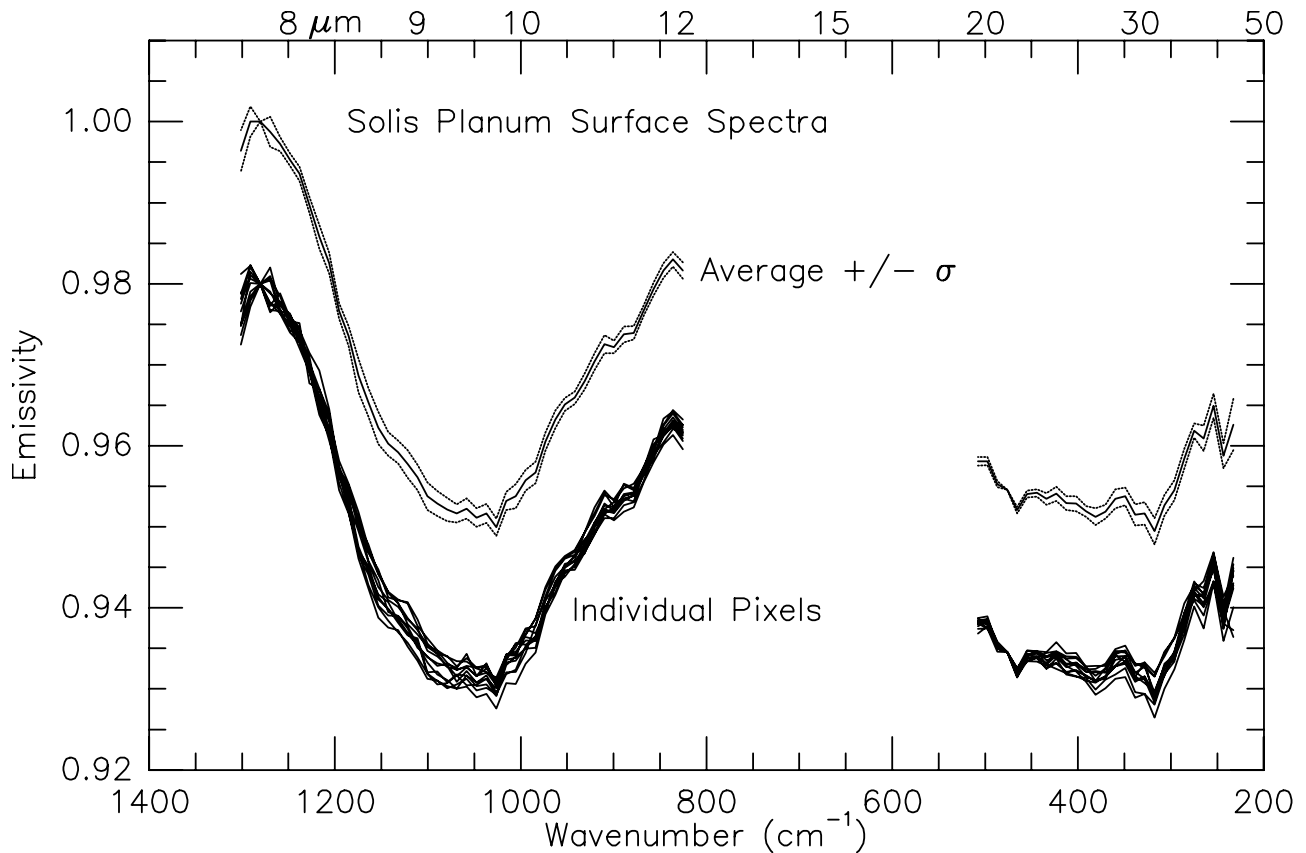


**Figure 4.** Solis Planum surface spectra from the area covering  $24^{\circ}$ – $27^{\circ}$ S and  $96^{\circ}$ – $98^{\circ}$ W. Individual binned pixels (offset by 0.02) are normalized to the average spectral contrast. The average (thick solid) is shown with the standard deviation (dotted) of the normalized individual pixels.

northern hemisphere low-albedo regions, which have some surfaces with concentrations of 0.05–0.10. These locations are not above the detection limit, and as discussed in the uncertainties section, the absence of hematite in these regions has been verified by other techniques.

### 3.1.6. Basaltic glass

[42] Basaltic glass has the highest concentrations within the central Acidalia region with several pixels approaching 0.10 concentrations (Figure 2a). There are several locations of slightly increased concentration in northern hemisphere low-albedo regions. Concentrations of 0–0.05 are common throughout low-albedo equatorial surfaces with isolated pixels displaying concentrations  $>0.05$ . Outside of these regions, low-Si glass concentrations are  $<0.02$ . There are no detectable concentrations of basaltic glass reported here.

### 3.1.7. Olivine

[43] Olivine concentrations are not above the detectable limit anywhere on the map (Figure 2a). Several areas consist of slightly elevated concentrations ( $\sim 0.02$ – $0.05$ ), including areas coincident with high concentrations of hematite as well as an isolated region within northeastern Syrtis Major and a low-albedo region immediately north of Argyre Basin. Several isolated pixels also display slightly higher concentrations in the far south.

### 3.1.8. Sulfates

[44] Sulfate concentrations are common throughout equatorial low-albedo regions, Acidalia, and the north polar sand seas at 0.05–0.10 (Figure 2b). These concentrations are

present but more sporadic in other low-albedo regions. Concentrations just above 0.10 are present in several pixels within Acidalia. High-albedo regions are dominated by concentrations of 0–0.05. Only several pixels within Acidalia are slightly above the detection limit.

### 3.1.9. Carbonates

[45] Carbonate minerals are not above the detection limit anywhere on the map ( $<0.10$ ; Figure 2b). Most areas are dominated by concentrations of 0–5% with the exception of equatorial low-albedo regions. These surfaces commonly indicate concentrations of 0.05–0.07. As discussed in the uncertainties section, other methods indicate that the actual concentrations are significantly lower in these regions. The  $\sim 1500$   $\text{cm}^{-1}$  band is outside the spectral region of this algorithm, and the  $\sim 350$  and  $\sim 890$   $\text{cm}^{-1}$  absorptions are being used at a low level to fit systematic errors in the data or in the atmospheric correction algorithm.

### 3.1.10. Quartz/amphibole

[46] Quartz and amphibole are not identified above the detection limit in any areas covered by this study (Figure 2b). Most surfaces are dominated by concentrations of 0–0.01 of each of these mineral classes. Several separate, isolated regions have concentrations of each mineral group of 0.01–0.02.

## 3.2. Distinctive Regions

[47] Several local or regional compositions are immediately discernible from the RMS error and mineral concen-

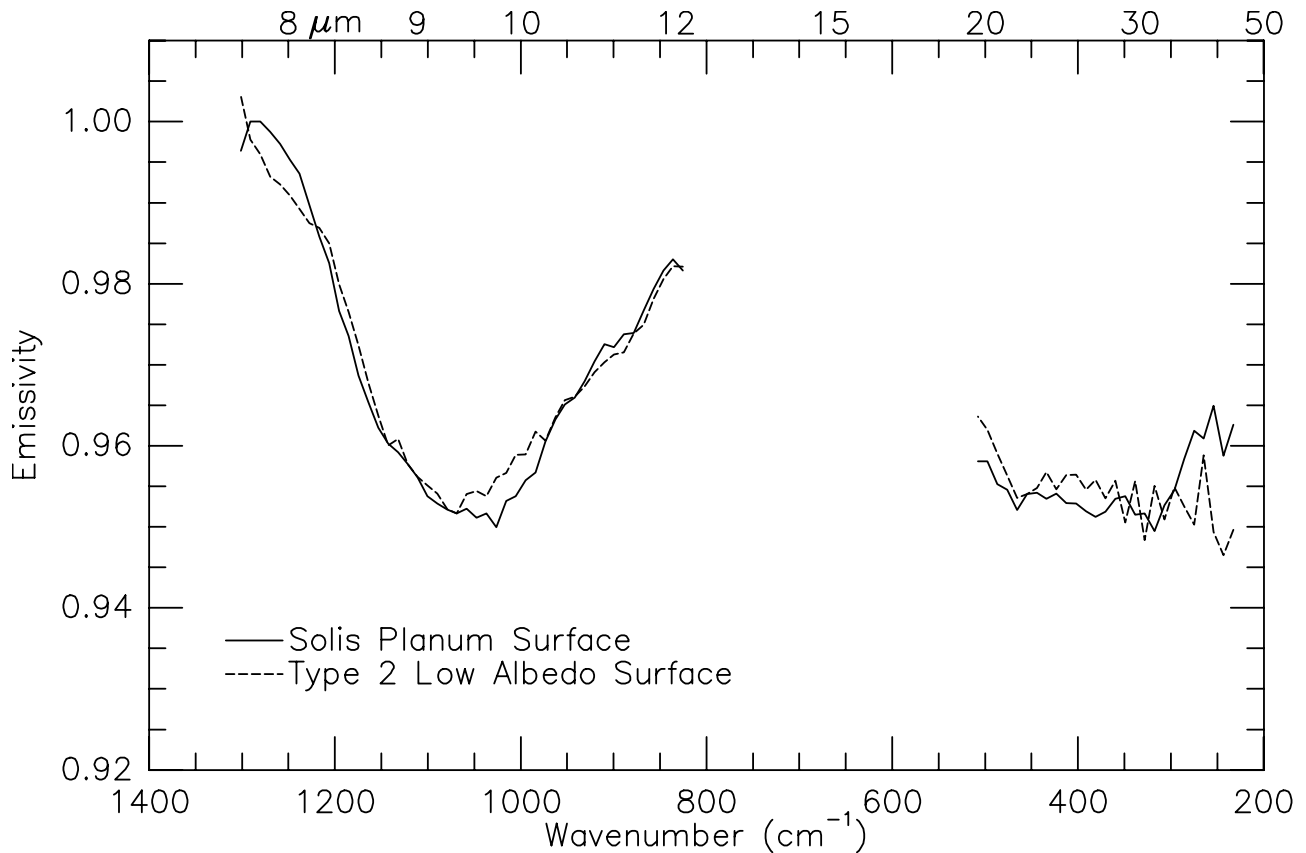


**Figure 5.** Average Solis Planum surface spectrum (solid) and best fit of the Type 2 low-albedo andesitic surface of *Bandfield et al.* [2000b] (dashed).

tration images that have not been identified in previous studies. Three different examples are shown here.

### 3.2.1. Solis Planum

[48] The sheet silicate and high-Si glass image (Figure 2a) displays several localized surfaces of elevated concentrations in the southern hemisphere, most notably an isolated region within Solis Planum (97°W, 25°S) where several pixels have values  $>0.20$ . Twelve binned and averaged TES emissivity spectra were taken from pixels in this region with elevated sheet silicate and glass concentrations (Figure 4). Pixels were selected to minimize atmospheric dust and water ice opacities ( $\tau_{\text{dust}} \approx 0.10-0.15$ ,  $\tau_{\text{ice}} < 0.05$ ), and no unusual artifacts appear to be present. Surface spectral contrast is relatively high with a minimum emissivity of  $\sim 0.95$  at  $1050 \text{ cm}^{-1}$ . The surface spectra were normalized to the average emissivity at  $1300 \text{ cm}^{-1}$  and  $500 \text{ cm}^{-1}$  to calculate the standard deviation in the spectral shape, which is an average of 0.0011. The surface spectral shape is compared to the andesitic spectrum of *Bandfield et al.* [2000a] (Figure 5). Though the overall character and shape of the two spectra are similar, there are several spectral regions where the two spectra are different. The trough of the  $\sim 1000 \text{ cm}^{-1}$  absorption is significantly broader and more rounded in the Solis Planum spectra. The steep slope at  $\sim 500 \text{ cm}^{-1}$  is also not as pronounced in the new spectra presented here. Discrepancies are also present at the extreme portions of the spectrum covered by this analysis. These discrepancies are coincident with  $\text{CO}_2$  isotope bands at high wave numbers and water vapor rotational absorptions at low wave numbers, however. Mineral end-member

concentrations do not differ significantly from those of *Bandfield et al.* [2000a].

### 3.2.2. High RMS errors

[49] Several locations of anomalously high RMS error were identified and investigated within two high-albedo regions near 294°W, 40°N and 170°W, 40°N. No adverse temperature or spectral artifact conditions are present in the binned TES spectra (Figure 6), and atmospheric particulate opacities are low ( $\tau_{\text{dust}} \approx 0.10-0.15$ ,  $\tau_{\text{ice}} < 0.05$ ). The least squares fit spectrum consistently deviates significantly ( $>0.005$  emissivity) from the average measured spectrum in the  $1200-1300 \text{ cm}^{-1}$  wave number region (Figure 7). A high-albedo, relatively low RMS error ( $\sim 0.0025$  versus  $\sim 0.0045$  RMS error in emissivity) region was selected to investigate the distinction between the two high-albedo surfaces. The residuals between measured and modeled spectra in both cases are similar in spectral character and magnitude with the exception that the high-albedo surface with the larger RMS error has higher magnitudes between  $\sim 1200$  and  $1300 \text{ cm}^{-1}$ . When this wavelength region is excluded from the least squares fit, RMS errors drop significantly from 0.0044 to 0.0022 and 0.237 to 0.0016 for the high and low RMS error high-albedo surfaces, respectively. In all cases, surface spectral contrast is low, and no minerals are near the detection limit (Table 2).

### 3.2.3. Southern hemisphere andesite

[50] Low albedo surfaces south of  $\sim 40^\circ\text{S}$  display significant concentrations of plagioclase feldspar and sheet silicates and/or high-Si glass with low concentrations of

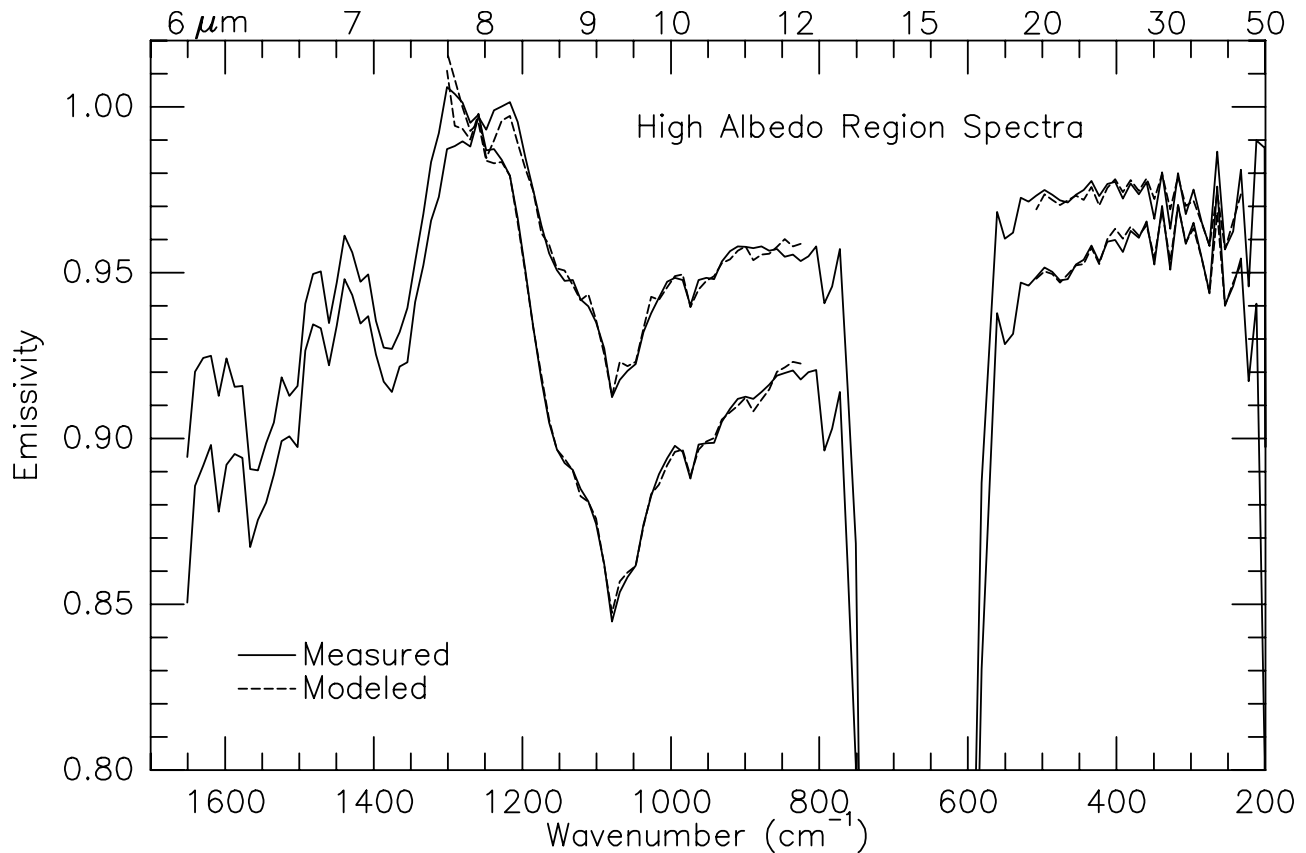


**Figure 6.** High-albedo region measured (solid) and modeled (dashed) TES spectra. The TES spectrum with less atmospheric dust absorption at  $\sim 1075 \text{ cm}^{-1}$  has significantly higher RMS error (0.00462 versus 0.00242 in emissivity) despite its very low dust opacity ( $\tau \approx 0.1$  versus 0.2). The low dust opacity spectrum is a binned pixel from Arabia Terra and the higher dust opacity spectrum is from Amazonis Planitia, and they are listed in Table 3.

other mineral groups, including high-Ca pyroxene (Figure 2). To ensure warm surfaces with low dust opacities, spectra were investigated within individual orbits rather than the binned maps (Table 2). The disappointingly quiet 2000 dust storm season on Mars provided a window of low dust opacity and high surface temperatures in the high latitudes within the southern hemisphere from heliocentric longitudes ( $L_s$ ) of  $\sim 250^\circ$ – $325^\circ$ . Several dozen to several hundred spectra with atmospheric dust opacities of  $\sim 0.15$ – $0.20$  and no detectable water ice were averaged in each case from a spectrally homogeneous low-albedo surface. RMS error between measured and modeled spectra is low at an average of 0.0029 in emissivity, and all spectral features are reproduced well. Surface spectra vary in spectral contrast with  $1050 \text{ cm}^{-1}$  emissivities of  $\sim 0.94$ – $0.97$ . Surface spectra were normalized and standard deviations were calculated in a similar manner as discussed above to investigate spectral shape (Figures 8 and 9). Accounting for an average standard deviation of 0.0020, spectral shape is nearly identical to that of the Type 2 spectrum of *Bandfield et al.* [2000a] with the largest differences at the extreme wave numbers of the analysis that are coincident with atmospheric  $\text{CO}_2$  and water vapor absorptions. End-member concentrations do not differ significantly from the andesitic surface spectral type of *Bandfield et al.* [2000a]; however, surface spectral contrast is significantly lower with an average  $1050 \text{ cm}^{-1}$

emissivity of 0.965 versus 0.945 for the andesite spectral type.

#### 4. Discussion

[51] No surface on the planet is dominated by any single mineral. All of the mineral maps must be taken into account in order to give an accurate impression of surface composition. The suite of materials present and their relative concentrations are necessary to identify rock type and conditions of genesis. This necessarily assumes that the surface is a single lithology and has not been subject to mixing due to limited spatial resolution or physical processes such as mixing of sand sources. The individual maps facilitate the location of unique areas such as those with hematite present.

[52] Several representative pixels from different surface types were isolated, and their mineral concentrations are listed in Table 3. These concentrations are normalized to sum to 100% to better determine the rock type and to compare with previous results. The normalized percentages represent the areal coverage of the mineralogy of the coarse particulate surface. It must be assumed that the normalized concentrations represent the volumetric abundance to determine rock type and to compare to bulk mineral abundances derived from thin section techniques. Pixels were chosen

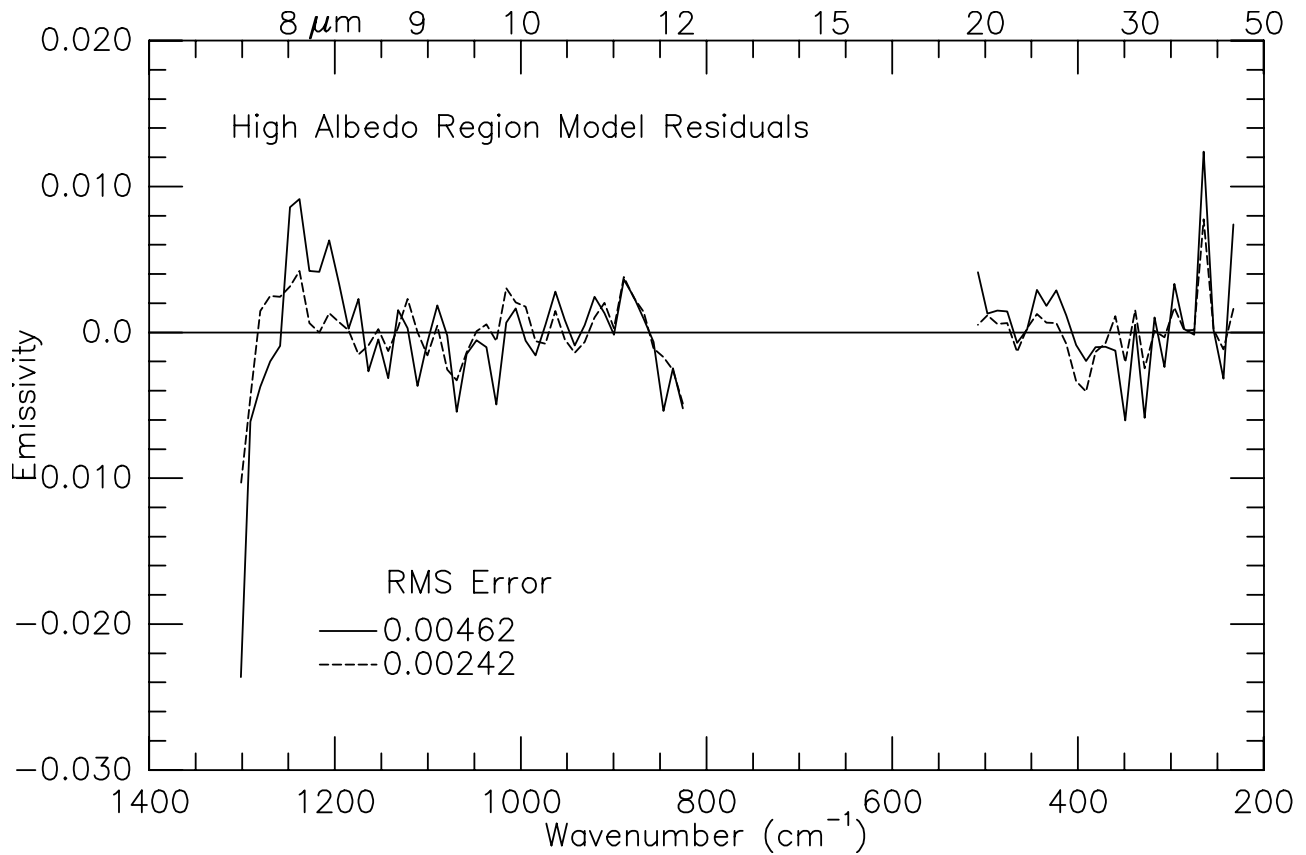


**Figure 7.** Residual errors for the two high-albedo region spectra from Arabia Terra (solid) and Amazonis Planitia (dashed). The presence of fine particulate silicate surfaces within high-albedo regions and the lack of fine particulate end-members in the model prevent an adequate fit at  $<1200\text{ cm}^{-1}$ , where deep surface absorptions are present. The character of the residual is similar between both regions but more intense within Arabia Terra.

from the distinctive regions discussed above, regions characterized as basaltic and andesitic by *Bandfield et al.* [2000a], as well as a hematite-rich area [*Christensen et al.*, 2000c, 2001b]. These include a high-albedo region with relatively high RMS error from northeast Arabia Terra; a high-albedo region with a lower RMS error from southern Amazonis Planitia; an andesitic region from northern Acidalia Planitia; a basaltic region from central Syrtis Major; a high-latitude, low-albedo region pixel from southern Noachis Terra; a pixel from the unique Solis Planum region; and a hematite-rich pixel from Sinus Meridiani. These pixels will be used for comparison in this discussion.

#### 4.1. Igneous Compositions and Distributions

[53] The results presented here are in good agreement with those of *Bandfield et al.* [2000a]. Table 4 lists the normalized concentrations of minerals reported by *Bandfield et al.* [2000b] in the same form as in Table 3 for comparison. The previously reported basaltic (Type 1) mineralogies are similar to those of the Syrtis Major pixel and are well within the uncertainties of both studies. One area of discrepancy is the relatively high (0.09), though still below the detection limit, carbonate concentration reported here. The previously reported mineralogy is from a much greater average and similar but slightly more precise technique than that applied here and is considered more accu-

rate. The greater accuracy of the previous study, along with other results as discussed in the error analysis section, indicates that carbonates are indeed not detected. The Syrtis Major pixel has a mineralogy dominated by intermediate plagioclase and high-Ca pyroxene and is indicative of a typical terrestrial basalt or low silica basaltic andesite [*Wyatt et al.*, 2001].

[54] The distributions of basaltic compositions (regions with both significant high-Ca pyroxene and high plagioclase concentrations) on the surface are in general agreement with previous results [*Bandfield et al.*, 2000a]. Significant concentrations of both of these mineral groups are present only in southern highlands regions. High-resolution studies of

**Table 2.** Data Used for Surface Spectrum Retrieval in Low-Albedo, High-Latitude Southern Hemisphere Regions

Orbit	Latitude, deg	Longitude, deg	$L_s$ , deg	$T$ , K
3529	-49	63	268	297
3615	-60	2	272	295
3628	-60	14	273	294
3653	-53	11	274	296
3670	-59	136	275	293
3867	-57	16	285	293
3903	-66	323	287	285
3959	-61	128	290	289
4369	-56	345	310	285

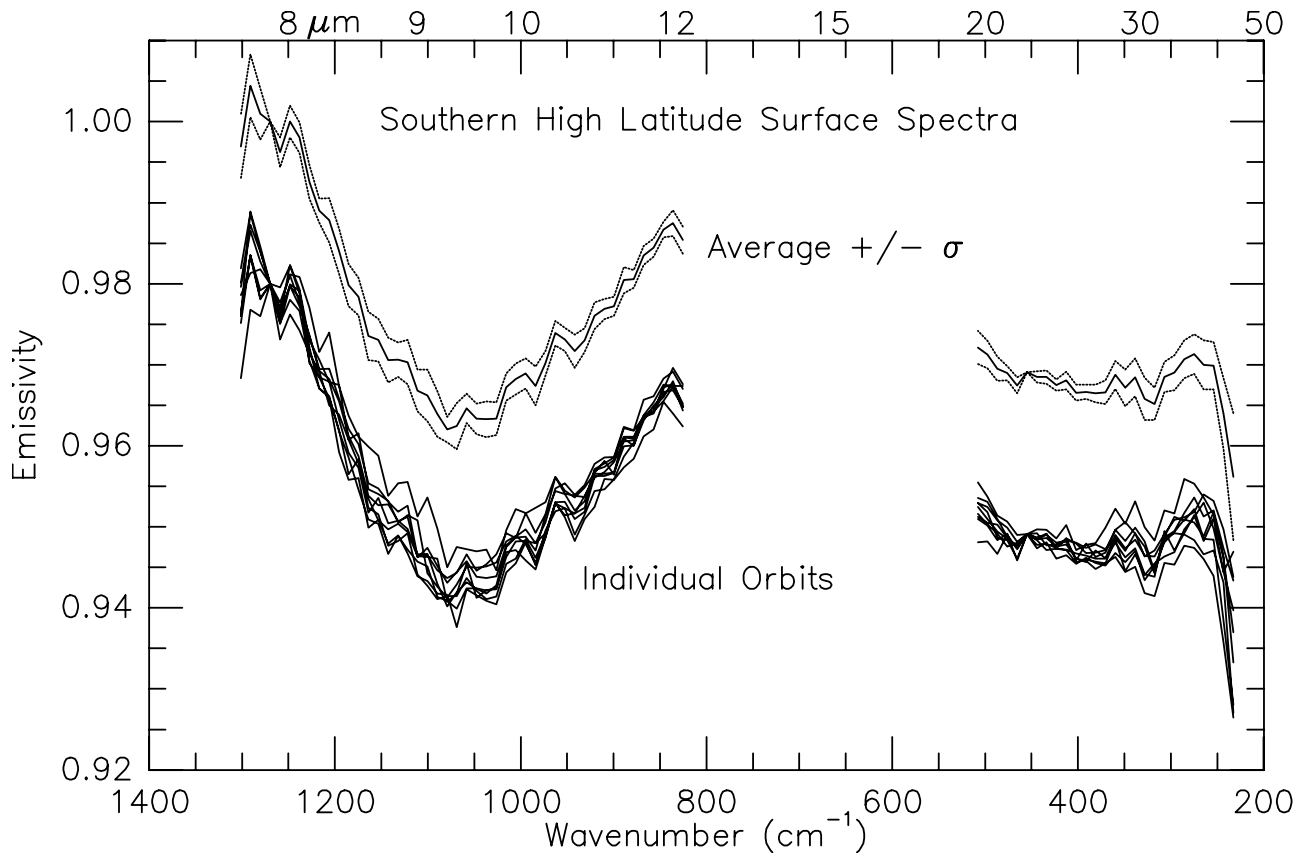


**Figure 8.** Southern hemisphere high-latitude, low-albedo surface spectra from nine individual orbits (Table 2). Individual surface retrievals (offset by 0.02) are normalized to the average spectral contrast. The average (thick solid) is shown with the standard deviation (dotted) of the normalized individual pixels.

basaltic component distributions have located these materials, with a few isolated and notable exceptions, exclusively in the southern highlands [Rogers *et al.*, 2001]. High-Ca pyroxene concentrations drop considerably relative to plagioclase at latitudes south of  $\sim 40^\circ\text{S}$ . This indicates a significant drop in the abundance of basalt on these surfaces. The highest concentrations of basalt are restricted to equatorial to midlatitude southern highlands regions.

[55] Three pixels representing distinct geographic locations have material concentrations that are similar to the andesitic (Type 2) composition reported by Bandfield *et al.* [2000a]. Sheet silicates and high-Si glass and plagioclase feldspar dominate these surfaces. Also indicated below the detection limit are both orthopyroxenes and high-Ca pyroxene and small amounts of sulfates, carbonates, and, in one instance, hematite. The results are all in good agreement with the previously reported compositions, though the Acidalia pixel has a slightly lower sheet silicate and high-Si glass concentration than previously reported. This is within the uncertainties of both techniques, especially after taking into account the normalization of the Acidalia pixel concentrations. These pixel mineralogies are representative of andesitic rocks dominated by intermediate plagioclase feldspar and silica-rich volcanic glass.

[56] This study does not discern between high-Si glass and sheet silicates because of their spectral similarity and

the relative coarseness of the manner in which the techniques are applied. As a result, the andesitic surfaces may instead represent a separate composition dominated by plagioclase feldspars and weathering products. There are several observations that make this scenario unlikely.

[57] Bandfield *et al.* [2000a] did discern between sheet silicates and high-Si glass using both deconvolution results as well as distinct features present in the Martian surface spectra. Oxidized and clay varnishes, though similar in character to high-Si glass, do not reproduce the features present in the Martian surface spectra, especially the steep negative slope present at  $\sim 500\text{ cm}^{-1}$  (see Figure 5). Although this feature is near the  $667\text{ cm}^{-1}$   $\text{CO}_2$  fundamental, the confidence in its presence is high, and any systematic error present would increase its prominence, as the last 2–3 spectral samples near the cutoff at  $\sim 530\text{ cm}^{-1}$  would be artificially depressed by minor  $\text{CO}_2$  absorption on the wing of the band.

[58] These surfaces have both the spectral contrast and thermal inertias consistent with sand-sized particles [Christensen, 1982, 1986; Bandfield *et al.*, 2000a], and both Viking and MOC images display active dune processes as well [Thomas, 1984; Edgett and Christensen, 1991; Thomas *et al.*, 1999], especially in the north polar sand seas that have these spectral signatures. Large abundances of weathering products are not common in eolian sands of a variety of dune fields. In addition, though surfaces of dark regions

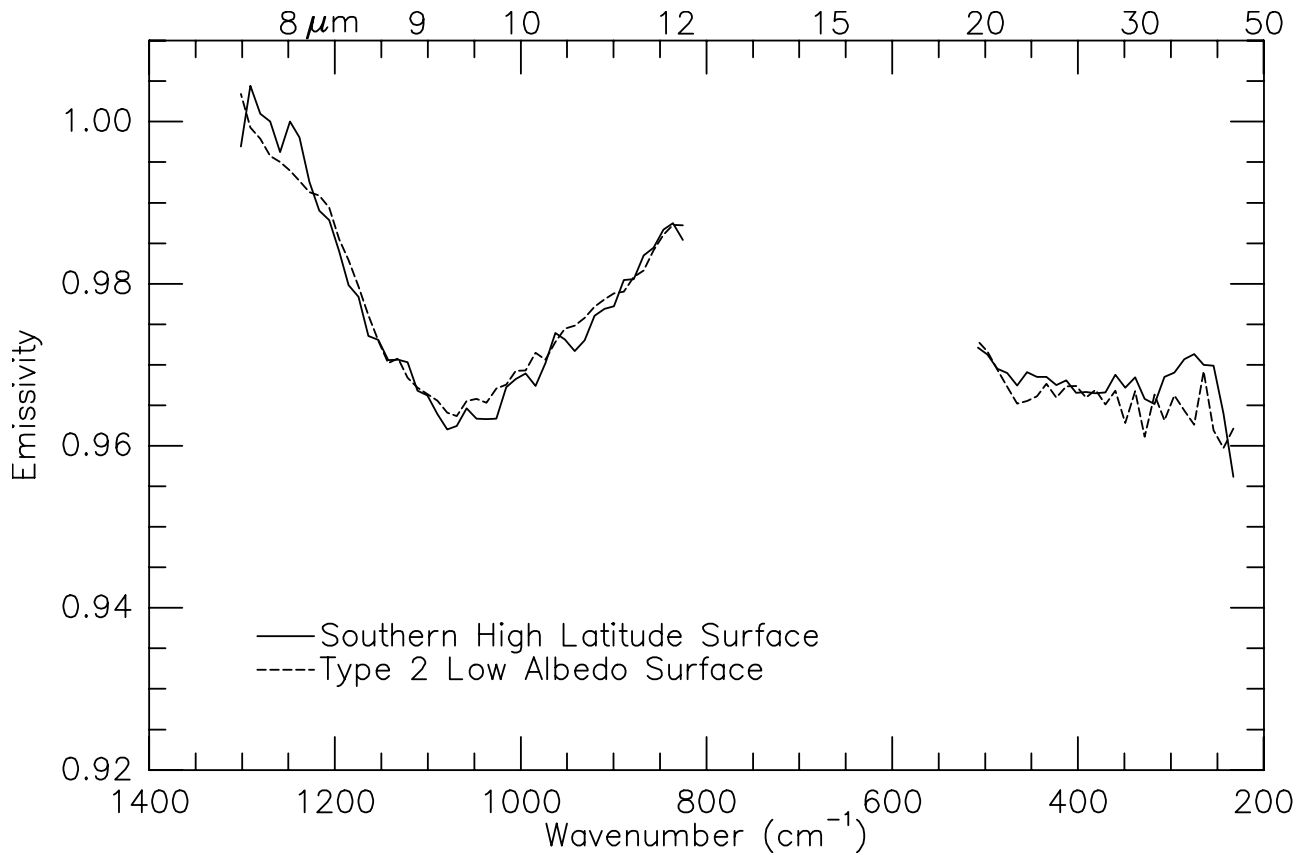


**Figure 9.** Average southern hemisphere high-latitude surface spectrum (solid) and best fit of the Type 2 low-albedo andesitic surface of *Bandfield et al.* [2000b] (dashed).

clearly show a red color, indicating the presence of small amounts (less than  $\sim 5\%$ ) of alteration products [Bell, 1996], significant abundances of altered minerals are not consistent with previous spectroscopic observations.

[59] Surfaces interpreted to be andesitic in composition by *Bandfield et al.* [2000a] are similar to surfaces where the mineral maps display high concentrations of both plagioclase and sheet silicates and high-Si glass. The highest concentrations of both mineral groups combined are located in the northern lowlands low-albedo regions such as Acidalia and the north polar sand seas. With an exception discussed below, more moderate concentrations

are located in equatorial and southern hemisphere low-albedo surfaces.

[60] An isolated location of several hundred kilometers in diameter near  $98^\circ\text{W}$ ,  $25^\circ\text{S}$  within Solis Planum displays high concentrations of both plagioclase and sheet silicates and high-Si glass. As shown in Figure 5 and Table 3, this surface is similar in spectral shape and end-member concentrations to the other regions, such as Acidalia, interpreted to be andesitic in composition. However, as discussed above, the spectral shape does contain small but significant differences from the other andesitic surfaces even though this does not relate to significant differences in derived

**Table 3.** Mineral Concentrations for Representative Pixels<sup>a</sup>

	Group/Region													
	Arabia		Amazonis		Syrtis		Acidalia		Noachis		Solis		Sinus	
Quartz					0.01	1%	0.01	2%						
K-feldspar	0.05	–	0.03	–	0.01	1	0.03	5	0.03	7%	0.01	2%	0.06	12%
Plagioclase			0.02	–	0.27	35	0.16	26	0.13	28	0.12	26	0.08	16
Amphibole					0.03	4								
Low-Ca pyroxene					0.04	5	0.06	10	0.02	4	0.02	4	0.01	2
Hi-Ca pyroxene					0.20	26	0.04	6	0.05	11	0.04	9	0.06	12
Olivine														
Sheet/high-Si glass	0.02	–	0.06	–	0.06	8	0.17	27	0.17	37	0.20	43	0.04	8
Low-Si glass													0.01	2
Oxide					0.02	3	0.04	6					0.14	29
Sulfate	0.01	–	0.02	–	0.04	5	0.07	11	0.04	9	0.04	9	0.06	12
Carbonate			0.02	–	0.09	12	0.04	6	0.02	4	0.04	9	0.03	6
RMS error, %	0.46		0.24		0.15		0.23		0.16		0.12		0.17	

<sup>a</sup>The first column is the actual retrieved concentration, and the second column is the normalized abundance.

**Table 4.** Normalized Mineral Abundances of Low-Albedo Surfaces from *Bandfield et al.* [2000b] and Martian Meteorite Los Angeles From *Rubin et al.* [2000]

Group/Region	Type 1	Type 2	Los Angeles
Quartz			
K-feldspar	6%	3%	2%
Plagioclase	43	27	46
Amphibole		6	
Low-Ca pyroxene	5	2	39 <sup>a</sup>
High-Ca pyroxene	24	8	39 <sup>a</sup>
Olivine		3	3
Sheet/high-Si glass	10	40	6
Low-Si glass			
Oxide			
Sulfate	2	5	
Carbonate	1	3	
RMS error	0.46	0.24	

<sup>a</sup>Pyroxene compositions in Los Angeles are primarily augite and pigeonite. *Rubin et al.* [2000] do not distinguish these minerals in their modal analysis.

mineralogy. Though still classified as andesitic in composition, these differences as well as its isolation from other surfaces of similar composition make this area unique.

[61] Low-resolution images display no relation between composition and surface morphology. The region appears smooth with numerous graben present that radiate from the Tharsis province to the northwest (Figure 10a). Rough, heavily cratered terrain is located immediately southwest of the region of interest but does not show any clear relation with it. No morphological boundaries are apparent that would distinguish the spectrally distinctive surface within the Solis Planum region.

[62] A survey of high-resolution MOC images within the Solis Planum terrain that appears smooth in the low-resolution Viking mosaic image reveals an extremely rough surface on the scale of several to tens of meters (Figure 10b) [*Malin and Edgett*, 2001]. Numerous small craters are present, and many appear subdued and eroded. There is no distinction in surface morphology between high-resolution images within and outside of the distinctive spectral unit. The high-resolution MOC images only coincided with localities of low to moderate concentrations of the distinctive spectral features, however.

[63] It is unlikely that this surface is mineralogically the same as other andesitic spectral regions with a small amount of an independent composition locally mixed in. The spectral shape is extremely constant (Figure 4), and its location is isolated from other high concentrations of andesite materials. The brief view of context images displays nothing to distinguish this area from its immediate surroundings. Thermal inertia is moderate ( $\sim 200\text{--}350 \text{ J m}^{-2} \text{ K}^{-1} \text{ s}^{-1/2}$ ) [*Mellon et al.*, 2000] and is also not distinct from the surrounding area. A more detailed study of available data sets is necessary to characterize this region, including high-resolution thermal inertia and mineral concentration maps as well as a thorough investigation of high-resolution imagery.

[64] Significant concentrations of materials indistinguishable from andesitic surfaces in the northern hemisphere low-albedo regions are present at high latitudes in southern hemisphere, low-albedo regions (Figure 9, Table 3). Both the spectral signature and derived mineralogies are well within the uncertainties of the andesitic surface of *Bandfield*

*et al.* [2000a] and have little, if any, character of the basaltic surface. This indicates a transition to andesitic surfaces at high latitudes in the southern hemisphere. The basaltic surfaces roughly form a southern equatorial band capped with andesitic surfaces at midlatitudes and high latitudes. The transition from basaltic to andesitic surfaces appears gradual with no obvious distinguishing boundaries, such as the dichotomy boundary to the north.

[65] These distributions are perplexing as much as they are surprising. The Earth and the Moon have fundamental but very different mechanisms responsible for striking global distributions of surface compositions. These two data points might not suggest that an intermediate-sized planet should have a homogeneous and simply basaltic surface. However, there is no plausible process offered here to explain the distributions of compositions on Mars, and it is unclear if there are distinct mechanisms responsible for the distributions of the two compositions. Andesite formation appears to be independent of crustal thickness [*Zuber et al.*, 2000] and age, and basaltic surfaces are still restricted to generally older heavily cratered surfaces.

[66] Though the spectral shapes and relative mineral abundances may not be distinguished, the spectral contrast as well as absolute mineral concentrations are significantly smaller in these southern hemisphere regions. This suggests that a spectrally inert component, such as dust, might be intermixed. The coverage of the andesite and inert components is estimated to be 70 and 30%, respectively, from the relative spectral contrasts between the southern hemisphere andesite surfaces and the deeper contrast surfaces found in the northern hemisphere. This estimate assumes that the particle size and surface texture of the andesite are similar to those of surfaces with complete coverage such as the northern circumpolar sand seas. Thermal inertia as well as spectral data suggest that many surfaces in the southern hemisphere may be indurated [*Christensen and Moore*, 1992; *Mellon et al.*, 2000; *Ruff and Christensen*, 2001]. These indurated surfaces have spectral signatures with emissivities close to unity that might contribute to the shallow spectrum [*Ruff et al.*, 2001].

## 4.2. Mineral Compositions and Distributions

### 4.2.1. Feldspar and pyroxene

[67] Feldspar compositions are dominated by intermediate to calcic plagioclase. Though plagioclase composition alone is not a good indicator of rock type, these results are consistent with basaltic and andesitic surfaces. The lack of potassium feldspar and sodic feldspars, such as albite, suggests a general lack of large quantities of rocks bearing these minerals, such as granites. Higher precision in determining feldspar compositions is difficult even in the laboratory and, with the uncertainties stated here, would not be significant.

[68] The only pyroxenes identified above the detection limit were high-Ca clinopyroxenes within basaltic surface types. Concentrations below the detection limit are present elsewhere. Small concentrations of orthopyroxenes are commonly indicated but are not above the detection limit. The concentrations within andesitic and basaltic regions are consistent with, but not unique to, typical andesitic and basaltic volcanic rocks, respectively. Intermediate to mafic compositions may contain a wide range of pyroxene

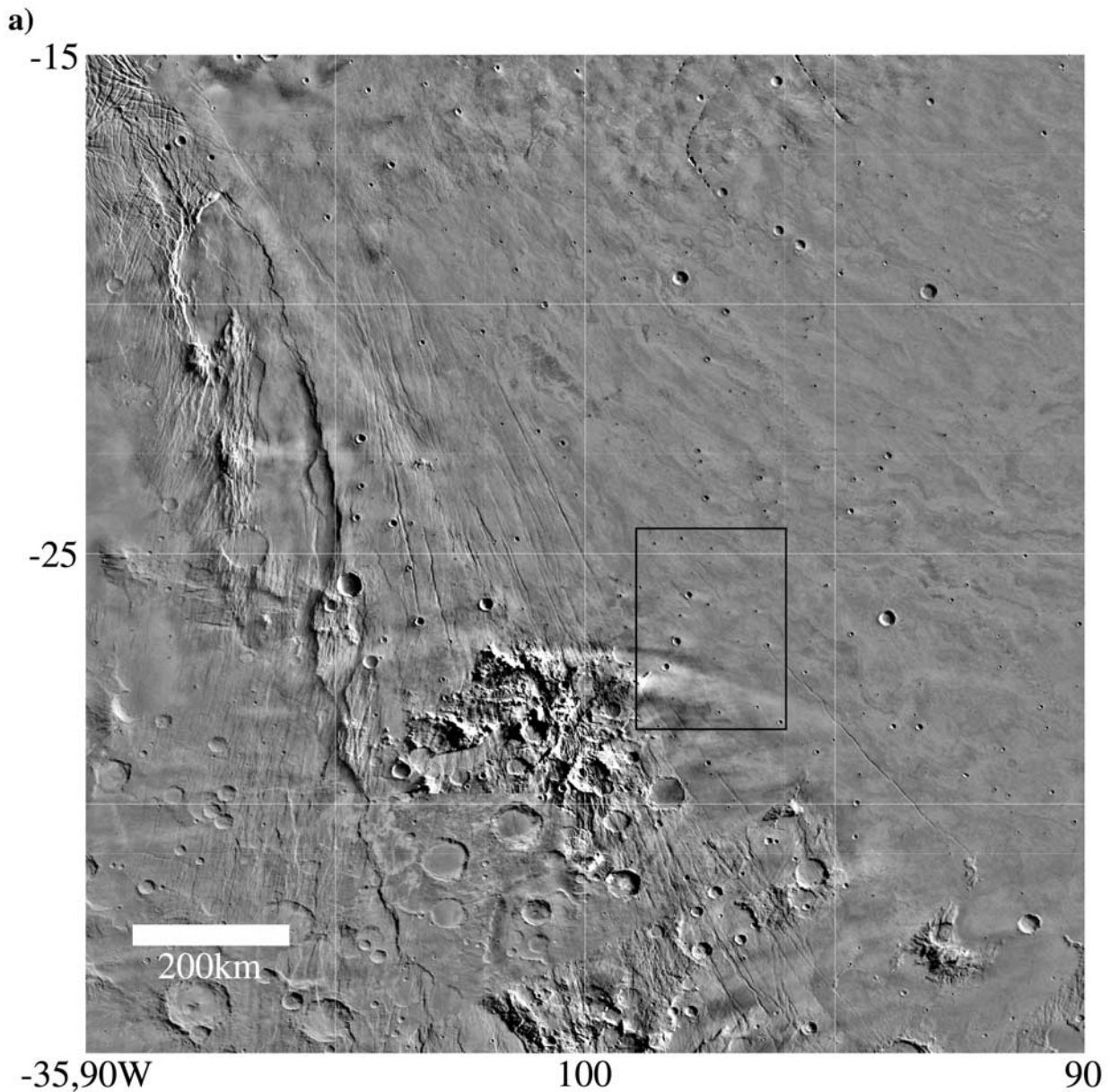


**Figure 10.** Regional and local images of Solis Planum. (a) Viking mosaic of the region. The highest concentrations of the unique spectral shapes shown in Figure 4 are located within the box centered roughly at  $27^{\circ}\text{S}$ ,  $97^{\circ}\text{W}$ . (b) Subset of MOC image M02-00849 centered at  $23.4^{\circ}\text{S}$ ,  $97.9^{\circ}\text{W}$ . The rough, cratered terrain is characteristic of regional surfaces that appear smooth at lower resolutions. Image resolution is 7 m/pixel.

compositions, which alone are not a good indicator of rock type for these compositions.

[69] The lack of a high-quality pigeonite end-member for this analysis presents some difficulty. Several Martian meteorites contain abundant pigeonite (see review by *McSween [1994]*), and VNIR studies have found  $\sim 1$  and  $2 \mu\text{m}$  absorption positions and shapes consistent with the presence of a pigeonite component [*Mustard et al., 1997*]. A study by *Hamilton et al. [1997]* using deconvolution methods on laboratory spectra of SNC meteorites could not adequately reproduce spectral features in meteorite samples with high pigeonite abundances, indicating that a pigeonite

end-member is required to model spectra of surfaces with high abundances of pigeonite. The low RMS errors and ability to model all spectral features in TES spectra without pigeonite suggests that it is not a major surface component.

[70] Both pyroxene and plagioclase compositions and normalized abundances do not match well with most Martian meteorite mineralogies. In addition, laboratory spectra of Martian meteorites that could be acquired are not representative of Martian surface spectra [*Christensen et al., 2000b; Hamilton et al., 2001a*]. This is not surprising, as most Martian meteorites are cumulates and are not necessarily representative of surface compositions. The

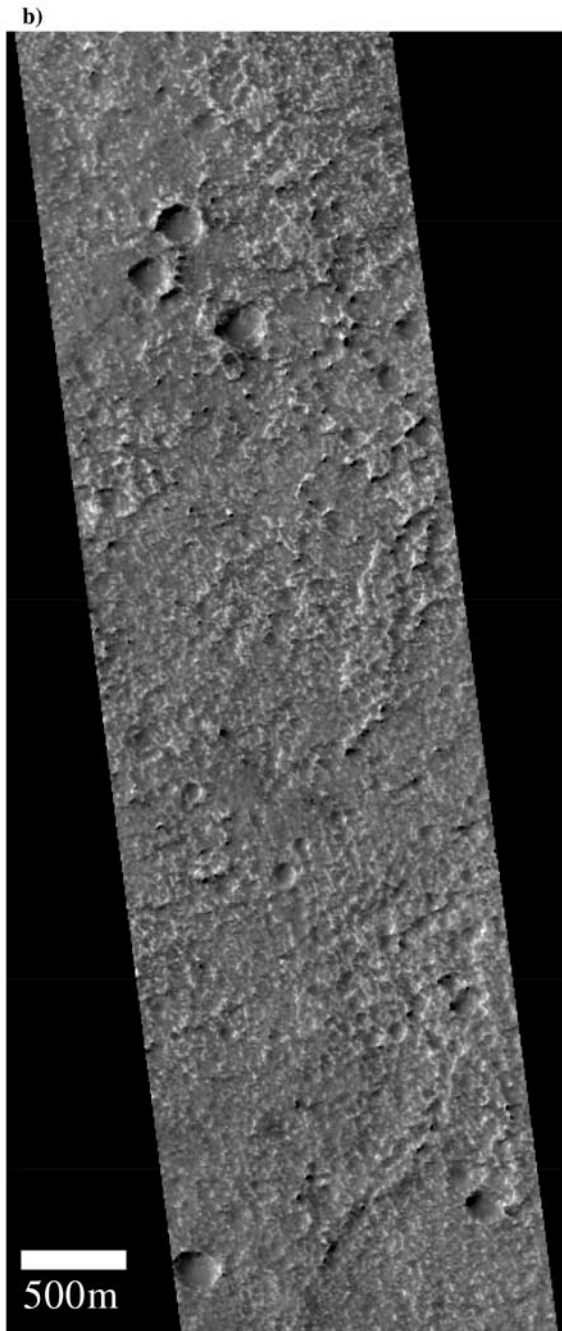


Figure 10. (continued)

basaltic shergottite meteorites are probably representative of at least near-surface volcanic compositions, however. Many basaltic shergottites have much higher low-Ca pyroxene and lower plagioclase abundances [McSween, 1994] than the normalized basaltic surface mineralogy derived here.

[71] Several basaltic shergottites do provide a better match to the basaltic surface composition, including QUE94201 and Los Angeles [Harvey *et al.*, 1996; Rubin *et al.*, 2000]. Both of these meteorites have higher Al contents and plagioclase abundances than other basaltic shergottites. Mineral abundances of Los Angeles (Table 4) agree within

uncertainty limits to the TES basaltic surface composition. However, pyroxene compositions in Los Angeles are dominated by pigeonite and augite, of which only augite is consistent with this and previous studies, though the relative abundance of each pyroxene was not reported. TES data are roughly consistent with basaltic shergottite Martian meteorites with high Al contents.

[72] The discrepancy between Martian meteorites and TES-derived surface compositions is not so much in the differences in mineralogy, but the difference in variety. Greater than 99% of Martian low-albedo regions may be described by two volcanic compositions. A very limited sample of probably much less than 1% of the Martian near surface with the basaltic shergottites has yielded a host of different mineralogies. It must be stressed, however, that TES is measuring surface sands that may be locally homogenized, whereas the Martian meteorites are sampling bedrock.

#### 4.2.2. Hematite

[73] The mineral maps discussed here do not approach the resolution of previous TES investigations of hematite [Christensen *et al.*, 2000a, 2001b]. They do provide confidence in the ability to identify new or unique surfaces using the deconvolution and atmospheric correction techniques on a broad scale and with a large suite of endmembers. Both the Aram Chaos and Sinus Meridiani regions are confidently identified as containing significant quantities of hematite, and the maps do not display any false positives above the 0.10 detection limit.

#### 4.2.3. Olivine

[74] Small quantities of olivine are identified in the mineral maps below the detection limit in Nili Fossae, Sinus Meridiani, and north of Argyre Basin. Other studies have detected unique spectral features present in TES data that closely match several olivine absorptions in both Nili Fossae and north of Argyre Basin [Hoefen and Clark, 2001; Hamilton *et al.*, 2001b]. The Sinus Meridiani olivine concentrations correspond to areas with high hematite concentrations, and there is no independent evidence for the presence of olivine in this region. In three of three cases presented here, the olivine map pointed out areas of unique composition and in two of three cases identified the correct mineral component even though it is identified below the detection limit. Though conclusive evidence of olivine is not present in its mineral map, it distinctly points to regions of interest. The low resolution of the mineral distribution maps and the local nature of the deposits prevent the positive identification at concentrations above the detection limit. High-resolution olivine mineral maps binned at 4 pixels per degree do identify significant quantities of olivine in Nili Fossae and north of Argyre Basin in isolated pixels at 0.10–0.15 concentrations consistent with the the 20–25% normalized abundances determined by Hamilton *et al.* [2001b].

#### 4.2.4. Sulfates/carbonate

[75] Neither sulfates nor carbonates are identified above the detection limit with the exception of several isolated pixels in Acidalia with sulfate concentrations at  $\sim 0.10$ – $0.11$ . As discussed above in the error analysis, carbonates may be identified by other methods that have restricted its possible concentrations to less than is shown here [Bandfield and Smith, 2001; Christensen *et al.*, 2001a]. Sulfates may be more

difficult to identify by visual inspection than deconvolution techniques as most have broad, relatively simple features near  $1150\text{ cm}^{-1}$  that would be superimposed on any silicate absorptions that might be present. Though technically slightly above the detection limit in several isolated pixels, there is little other evidence for sulfates when the atmospherically corrected spectra are inspected manually. The identification is not robust, and it remains premature to conclude the presence of sulfates on the Martian surface using TES data at this time. The method and results presented here are somewhat similar to those of *Cooper and Mustard* [2001], and again, the positive identification of sulfates is not robust. Significant abundances of sulfates may be present in the fine-grained dust, however, and would escape detection in this analysis.

[76] Both carbonates and sulfates have spatially coherent patterns that are coincident with low-albedo regions. This probably represents systematic error in the results, and slight amounts of each mineral are used to compensate for a discrepancy when fitting the TES spectra. Previous results by *Bandfield et al.* [2000a], which are considered more accurate, display lower concentrations of both mineral groups in low-albedo regions than are reported here. Spatially coherent patterns are necessary but not sufficient for a robust mineral identification.

#### 4.2.5. Sheet silicates

[77] Sheet silicates are difficult to positively distinguish from high-Si glass, as their general spectral similarity requires a higher precision than is present with this general view of the entire planet. Previous studies have identified minor amounts of sheet silicate materials at or near the detection limit [*Bandfield et al.*, 2000a; *Christensen et al.*, 2000b]. Though sheet silicates have not been positively identified by this study or previous studies, the derived concentrations represent 10–15% areal abundances. These areal abundances are consistent with thin coatings or altered surfaces that are possibly present and represent <1% volume abundances. As discussed in the results section, significant concentrations of high-Si glass have been identified and distinguished from sheet silicates previously [*Bandfield et al.*, 2000a] and are likely present where the sheet silicate and high-Si glass map displays high concentrations.

#### 4.2.6. Quartz/amphibole/basaltic glass

[78] The lack of significant quantities of quartz, amphibole, and basaltic glass agrees well with the results discussed above. Significant quantities ( $>0.10$ ) of quartz and amphibole would not be consistent with andesitic and basaltic compositions. Higher amounts of quartz could be present instead of, but not in addition to, the high concentrations of high-Si glass found in the andesitic surfaces. However, quartz and high-Si glass are easily distinguished spectrally, and the algorithm clearly favors high-Si glass over quartz. High-Si rock compositions (e.g., dacites and rhyolites) are not common on the Martian surface. The lack of high concentrations of basaltic glass suggests that quenching was not an important process in their formation.

### 4.3. High-Albedo Regions

[79] The spectral signature in high-albedo regions is not well modeled by coarse particulate materials, preventing the ability to recover accurate surface spectra using the decon-

volution method. The character of the measured versus modeled spectra does indicate the general character of spectra in light regions. Most of the spectral regions studied can be modeled closely with atmospheric spectral shapes alone [*Bandfield et al.*, 2000b], indicating a surface with low spectral contrast. The poor fit at short wavelengths, however, indicates the presence of strong surface absorption.

[80] This general spectral shape is consistent with fine-grained silicate materials. In fine-grained silicates, the  $\sim 500$  and  $1000\text{ cm}^{-1}$  Reststrahlen absorptions are considerably reduced in magnitude, and volume scattering effects are prominent at wavelengths short of the Christiansen frequency (greater than  $\sim 1300\text{ cm}^{-1}$ ). Any analysis of these surfaces must have atmospheric correction extended to the shortest wavelengths of TES as has been performed using a multiple emission angle surface-atmosphere separation technique [*Bandfield and Smith*, 2001]. In addition, compositional analysis using fine-grained thermal infrared spectra has not been studied extensively and is poorly understood.

[81] The relative depth of the short-wavelength absorption may be measured in TES emissivity spectra without any atmospheric correction applied to it. This absorption can be quite deep ( $\sim 0.9$  emissivity) and displays a very consistent spatial pattern of band depth that is correlated with regions of high albedo and low thermal inertia. *Ruff and Christensen* [2001] have mapped the depth of this absorption at  $1350\text{--}1400\text{ cm}^{-1}$  as a dust cover index. This index corresponds closely with the RMS error image reported here, including the Amazonis and Arabia regions that have both anomalously high RMS errors and prominent short wavelength absorptions. This indicates that dust-covered surfaces are primarily responsible for high RMS errors because of the lack of fine particulate end-members, preventing a retrieval of any significant mineralogy. While much has been learned about the physical character of dust-covered surfaces on Mars, existing methods and techniques are not sufficient to extract compositional information in the thermal infrared with confidence despite some initial studies [*Ramsey and Christensen*, 1998].

## 5. Conclusions

[82] The global maps summarized in this work show the regional surface material distributions on Mars. Exposed coarse particulate material is dominated by igneous mineralogies. Previous spectroscopic results along with the hematite maps and the possible presence of sheet silicate materials are evidence that alteration and precipitation of minerals have occurred and were or are common at some level. There is little evidence, however, of metamorphic compositions on a large scale. While these general compositions are not unexpected for Mars, their specific compositions and relative locations provide evidence for previously suspected and some unexpected processes, past and present, in the Martian interior and on its surface. Addressing what processes are responsible for the mineralogy of the Martian surface is beyond the scope of this paper. However, future studies will be able to use the compositions and their distributions presented here to help determine what these processes were.

[83] The work presented here has demonstrated the following:

- The only detectable pyroxene concentrations are high-Ca pyroxenes within low-latitude southern highlands regions. Smaller amounts of both low-Ca and high-Ca pyroxenes (<0.10 concentration) are identified in other low-albedo regions but are not above the detection limit.
- Plagioclase feldspar is identified in significant concentrations in all Martian low-albedo regions. No potassium feldspar is detected, and plagioclase compositions are intermediate to calcic.
- Sheet silicates and high-Si glass have the highest concentrations in northern hemisphere low-albedo regions. With several localized exceptions, lesser concentrations are identified in other low-albedo regions.
- Hematite is detected wherever previous, more intensive searches have detected it above the detection limit of this technique as applied to TES data. No areas were incorrectly identified as hematite rich.
- Consistent with other studies, carbonate concentrations are not present above the detection limit.
- Sulfate concentrations are present below the detection limit with the exception of several pixels within Acidalia that have sulfate concentrations just above the detection limit. There is little confidence in the actual detection of sulfates from this study based on inspection of the TES spectra.
- Olivine is identified below the detection limit in several isolated areas. In two of three instances, these concentrations are consistent with other studies that have identified olivine.
- Quartz, amphiboles, and basaltic glass are not identified above the detection limit in the 1 pixel per degree mineral maps.
- Mineral map distributions and normalized mineral abundances are in general agreement with previous studies. Distributions and mineralogies are consistent with the highest concentrations of andesitic surfaces in the northern lowlands and basaltic surfaces confined to the southern highlands.
- High-albedo regions do not display significant mineral concentrations. Regions of high RMS error in least squares fits correspond to areas of increased dust cover.
- High-latitude, low-albedo surfaces in the southern hemisphere have the same spectral signature as andesitic surfaces in the northern hemisphere. Spectral contrast is lower in the southern hemisphere than the north. Regional scale basaltic surfaces are confined to a “stripe” of southern highlands low and midlatitude surfaces.
- A localized area several hundred kilometers in diameter within Solis Planum has a distinct surface spectrum. The derived mineralogy of this region is not distinguishable from that of other surfaces with high plagioclase and high sheet silicate and high-Si glass concentrations. Low- and high-resolution images of this region do not point to any obvious source for this distinctive surface component.

[84] **Acknowledgments.** I would like to thank Mike Kraft and Mike Wyatt for useful reviews and discussions. Phil Christensen, John Pearl, and Mike Smith also provided helpful advice and discussions. Victoria Hamilton provided a formal review that significantly improved and clarified this manuscript. Thanks to Kelly Bender, Kim Murray, Kim Homan, Noel

Gorelick, and Sadaat Anwar at Arizona State University for their excellent planning, acquisition, processing, and software support of the TES data.

## References

- Adams, J. B., Lunar and Martian surfaces: Petrologic significance of absorption bands in the near-infrared, *Science*, 159, 1453–1455, 1968.
- Adams, J. B., Visible and near-infrared diffuse reflectance spectra of pyroxenes as applied to remote sensing of solid objects in the solar system, *J. Geophys. Res.*, 79, 4829–4836, 1974.
- Adams, J. B., and T. B. McCord, Mars: Interpretation of spectral reflectivity of light and dark regions, *J. Geophys. Res.*, 74, 4851–4856, 1969.
- Aronson, J. R., and A. G. Emslie, Composition of the Martian dust as derived by spectroscopy from Mariner 9, *J. Geophys. Res.*, 80, 4925–4931, 1975.
- Bandfield, J. L., and M. D. Smith, Multiple emission angle surface-atmosphere separations of MGS Thermal Emission Spectrometer data, *Lunar Planet. Sci.* [CD-ROM], XXXII, 1596, 2001.
- Bandfield, J. L., V. E. Hamilton, and P. R. Christensen, A global view of Martian surface compositions from MGS-TES, *Science*, 287, 1626–1630, 2000a.
- Bandfield, J. L., P. R. Christensen, and M. D. Smith, Spectral data set factor analysis and end-member recovery: Application to Martian atmospheric particulates, *J. Geophys. Res.*, 105, 9573–9588, 2000b.
- Bell, J. F., III, Iron, sulfate, carbonate, and hydrated minerals on Mars, in *Mineral Spectroscopy: A Tribute to Roger G. Burns*, edited by M. D. Dyar, C. McCammon, and M. W. Schaefer, *Spec. Publ. Geochem. Soc.*, 5, 359–380, 1996.
- Bell, J. F., III, and R. V. Morris, Identification of hematite on Mars from HST, *Lunar Planet. Sci.*, [CD-ROM], XXX, 1751, 1999.
- Bell, J. F., III, T. B. McCord, and P. D. Owensby, Observational evidence of crystalline iron oxides on Mars, *J. Geophys. Res.*, 95, 14,447–14,461, 1990.
- Bell, J. F., III, et al., Mineralogic and compositional properties of Martian soil and dust: Results from Mars Pathfinder, *J. Geophys. Res.*, 105, 1721–1755, 2000.
- Christensen, P. R., Martian dust mantling and surface composition: Interpretation of thermophysical properties, *J. Geophys. Res.*, 87, 9985–9998, 1982.
- Christensen, P. R., The spatial distribution of rocks on Mars, *Icarus*, 68, 217–238, 1986.
- Christensen, P. R., Variations in Martian surface composition and cloud occurrence determined from thermal infrared spectroscopy: Analysis of Viking and Mariner 9 data, *J. Geophys. Res.*, 103, 1733–1746, 1998.
- Christensen, P. R., and H. J. Moore, The Martian surface layer, in *Mars*, edited by H. H. Kieffer et al., pp. 686–729, Univ. of Ariz. Press, Tucson, 1992.
- Christensen, P. R., et al., Thermal Emission Spectrometer Experiment: Mars Observer Mission, *J. Geophys. Res.*, 97, 7719–7734, 1992.
- Christensen, P. R., et al., Detection of crystalline hematite mineralization on Mars by the Thermal Emission Spectrometer: Evidence for near-surface water, *J. Geophys. Res.*, 105, 9632–9642, 2000a.
- Christensen, P. R., J. L. Bandfield, M. D. Smith, V. E. Hamilton, and R. N. Clark, Identification of a basaltic component on the Martian surface from Thermal Emission Spectrometer data, *J. Geophys. Res.*, 105, 9609–9621, 2000b.
- Christensen, P. R., J. L. Bandfield, V. E. Hamilton, D. A. Howard, M. D. Lane, J. L. Piatek, S. W. Ruff, and W. L. Stefanov, A thermal emission spectral library of rock-forming minerals, *J. Geophys.*, 9735–9739, 2000c.
- Christensen, P. R., et al., The Mars Global Surveyor Thermal Emission Spectrometer experiment: Investigation description and surface science results, *J. Geophys. Res.*, 106, 23,823–23,871, 2001a.
- Christensen, P. R., R. V. Morris, M. D. Lane, J. L. Bandfield, and M. C. Malin, Global mapping of Martian hematite mineral deposits: Remnants of water-driven processes on Mars, *J. Geophys. Res.*, 106, 23,873–23,885, 2001b.
- Clancy, R. T., M. J. Wolff, and P. R. Christensen, MGS TES measurements of dust and ice aerosol behaviors, *Proc. Am. Astron. Soc. Div. Planet. Sci.*, 32, abstract 54.04, 2000.
- Clancy, R. T., S. W. Lee, G. R. Gladstone, W. W. McMillan, and T. Roush, A new model for Mars atmospheric dust based upon analysis of ultraviolet through infrared observations from Mariner 9, Viking, and Phobos, *J. Geophys. Res.*, 100, 5251–5263, 1995.
- Clark, B. C., A. K. Baird, R. J. Weldon, D. M. Tsusaki, L. Schnabel, and M. P. Candelaria, Chemical composition of Martian fines, *J. Geophys. Res.*, 87(B12), 10,059–10,067, 1982.
- Conrath, B., R. Curran, R. Hanel, V. Kunde, W. Maguire, J. Pearl, J. Pirraglia, and J. Welker, Atmospheric and surface properties of Mars obtained by infrared spectroscopy on Mariner 9, *J. Geophys. Res.*, 78, 4267–4278, 1973.

- Conrath, B. J., J. C. Pearl, M. D. Smith, W. C. Maguire, S. Dason, M. S. Kaelberer, and P. R. Christensen, Mars Global Surveyor Thermal Emission Spectrometer (TES) observations: Atmospheric temperatures during aerobraking and science phasing, *J. Geophys. Res.*, *105*, 9509–9519, 2000.
- Cooper, C. D., and J. F. Mustard, TES observations of the global distribution of sulfate on Mars, *Lunar Planet. Sci.* [CD-ROM] *XXXII*, 2048, 2001.
- Edgett, K. S., and P. R. Christensen, The particle size of Martian aeolian dunes, *J. Geophys. Res.*, *96*, 22,765–22,776, 1991.
- Feely, K. C., and P. R. Christensen, Quantitative compositional analysis using thermal emission spectroscopy: Application to igneous and metamorphic rocks, *J. Geophys. Res.*, *104*, 24,195–24,210, 1999.
- Geissler, P. E., R. B. Singer, G. Komatsu, S. Murchie, and J. Mustard, An unusual spectral unit in West Candor Chasma: Evidence for aqueous or hydrothermal alteration in the Martian canyons, *Icarus*, *106*, 380–391, 1993.
- Gillespie, A. R., Spectral mixture analysis of multispectral thermal infrared images, *Remote Sens. Environ.*, *42*, 137–145, 1992.
- Hamilton, V. E., and P. R. Christensen, Determining the modal mineralogy of mafic and ultramafic igneous rocks using thermal emission spectroscopy, *J. Geophys. Res.*, *105*, 9717–9733, 2000.
- Hamilton, V. E., P. R. Christensen, and H. Y. McSween Jr., Determination of Martian meteorite lithologies and mineralogies using vibrational spectroscopy, *J. Geophys. Res.*, *102*, 25,593–25,603, 1997.
- Hamilton, V. E., M. B. Wyatt, H. Y. McSween Jr., and P. R. Christensen, Analysis of terrestrial and volcanic compositions using thermal emission spectroscopy, 2, Application to Martian surface spectra from the Mars Global Surveyor Thermal Emission Spectrometer, *J. Geophys. Res.*, *106*, 14,733–14,746, 2001a.
- Hamilton, V. E., P. R. Christensen, H. Y. McSween Jr., R. N. Clark, and T. M. Hoefen, Spectral variations in MGS TES data of Nili Fossae: A possible source region for SNC meteorites on Mars?, *Lunar Planet. Sci.*, [CD-ROM], *XXXII*, 2184, 2001b.
- Harvey, R. P., T. J. McCoy, and L. A. Leshin, Shergottite QUE94201: Texture, mineral compositions, and comparison with other basaltic Shergottites, *Proc. Lunar Planet. Sci. Conf. 27th*, 497–498, 1996.
- Hoefen, T. M., and R. N. Clark, Compositional variability of Martian olivines using Mars Global Surveyor thermal emission spectra, *Lunar Planet. Sci.* [CD-ROM], *XXXII*, 2049, 2001.
- Hunt, G. R., L. M. Logan, and J. W. Salisbury, Mars: Components of infrared spectra and the composition of the dust cloud, *Icarus*, *18*, 459–469, 1973.
- Maguire, W. C., Martian isotopic ratios and upper limits for possible minor constituents as derived from Mariner 9 infrared spectrometer data, *Icarus*, *32*, 85–97, 1977.
- Malin, M. C., and K. S. Edgett, Mars Global Surveyor Mars Orbiter Camera: Interplanetary cruise through primary mission, *J. Geophys. Res.*, *106*, 23,429–23,570, 2001.
- Malin, M. C., et al., Early views of the Martian surface from the Mars Orbiter Camera of Mars Global Surveyor, *Science*, *279*, 1681–1685, 1998.
- Martin, T. Z., and M. I. Richardson, New dust opacity mapping from Viking IR Thermal Mapper data, *J. Geophys. Res.*, *98*, 10,941–10,949, 1993.
- McCord, T. B., R. N. Clark, and R. B. Singer, Mars: Near-infrared spectral reflectance of surface regions and compositional implications, *J. Geophys. Res.*, *87*, 3021–3032, 1982.
- McSween, H. Y., Jr., What have we learned about Mars from SNC meteorites?, *Meteoritics*, *29*, 757–779, 1994.
- Mellon, M. T., B. M. Jakosky, H. H. Kieffer, and P. R. Christensen, High-resolution thermal inertia mapping from the Mars Global Surveyor Thermal Emission Spectrometer, *Icarus*, *148*, 437–455, 2000.
- Merenyi, E., R. B. Singer, and J. S. Miller, Mapping of spectral variations on the surface of Mars from high resolution telescopic images, *Icarus*, *124*, 280–295, 1996.
- Morris, R. V., D. C. Golden, and J. F. Bell III, Low-temperature reflectivity spectra of red hematite and the color of Mars, *J. Geophys. Res.*, *102*, 9125–9133, 1997.
- Morris, R. V., et al., Mineralogy, composition, and alteration of Mars Pathfinder rocks and soils: Evidence from multispectral, elemental, and magnetic data of terrestrial analogue, SNC meteorite, and Pathfinder samples, *J. Geophys. Res.*, *105*, 1757–1817, 2000.
- Murchie, S., J. Mustard, J. Bishop, J. Head, C. Pieters, and S. Erard, Spatial variations in the spectral properties of bright regions on Mars, *Icarus*, *105*, 454–468, 1993.
- Mustard, J. F., S. Erard, J.-P. Bibring, J. W. Head, S. Hartz, Y. Langevin, C. M. Pieters, and C. J. Sotin, The surface of Syrtis Major: Composition of the volcanic substrate and mixing with altered dust and soil, *J. Geophys. Res.*, *98*, 3387–3400, 1993.
- Mustard, J. F., S. Murchie, S. Erard, and J. M. Sunshine, In situ compositions of Martian volcanics: Implications for the mantle, *J. Geophys. Res.*, *102*, 25,605–25,615, 1997.
- Ramsey, M. S., and J. H. Fink, Estimating silicic lava vesicularity with thermal remote sensing: A new technique for volcanic mapping and monitoring, *Bull. Volcanol.*, *61*, 32–39, 1999.
- Ramsey, M. S., and P. R. Christensen, Mineral abundance determination: Quantitative deconvolution of thermal emission spectra, *J. Geophys. Res.*, *103*, 577–596, 1998.
- Ramsey, M. S., P. R. Christensen, N. Lancaster, and D. A. Howard, Identification of sand sources and transport pathways at Kelso Dunes, California using thermal infrared remote sensing, *Geol. Soc. Am. Bull.*, *111*, 636–662, 1999.
- Rogers, D., P. R. Christensen, and J. L. Bandfield, Mars' volcanic surface compositions: distributions and boundaries using multiple orbiter datasets, *Lunar Planet. Sci.* [CD-ROM], *XXXII*, 2010, 2001.
- Rubin, A. E., P. H. Warren, J. P. Greenwood, R. S. Verish, L. A. Leshin, and R. L. Hervig, Petrology of Los Angeles: A new basaltic shergottite find, *Lunar Planet. Sci.* [CD-ROM], *XXXI*, 1963, 2000.
- Ruff, S. W., and P. R. Christensen, A spectrally based global dust cover index for Mars from Thermal Emission spectrometer data, paper presented at Mars Exploration Rovers Landing Site Workshop, Jet Propul. Lab., Pasadena, Calif., 2001.
- Ruff, S. W., P. R. Christensen, R. N. Clark, M. C. Malin, J. L. Bandfield, M. D. Lane, M. T. Mellon, and M. A. Prestley, Mars' "White Rock" feature lacks evidence of an aqueous origin, *J. Geophys. Res.*, *106*, 23,921–23,927, 2001.
- Singer, R. B., The dark materials on Mars, II, New mineralogic interpretations from reflectance spectroscopy and petrologic implications, *Proc. Lunar Planet. Sci. Conf. 11th*, 1048–1050, 1980.
- Singer, R. B., and H. Y. McSween Jr., The igneous crust of Mars: Compositional evidence from remote sensing and the SNC meteorites, in *Resources of Near-Earth Space*, edited by J. Lewis, M. S. Matthews, and M. L. Guerrieri, pp. 709–736, Univ. of Ariz. Press, Tucson, 1993.
- Singer, R. B., T. B. McCord, R. N. Clark, J. B. Adams, and R. L. Huguenin, Mars surface composition from reflectance spectroscopy: A summary, *J. Geophys. Res.*, *84*, 8415–8425, 1979.
- Smith, M. D., The annual cycle of water vapor on Mars as observed by the Thermal Emission Spectrometer, *J. Geophys. Res.*, *107*, 10.1029/2001JE001522, in press, 2002.
- Smith, M. D., J. L. Bandfield, and P. R. Christensen, Separation of atmospheric and surface spectral features in Mars Global Surveyor Thermal Emission Spectrometer (TES) spectra, *J. Geophys. Res.*, *105*, 9589–9607, 2000.
- Smith, M. D., J. C. Pearl, B. J. Conrath, and P. R. Christensen, Thermal Emission spectrometer results: Mars atmospheric thermal structure and aerosol distribution, *J. Geophys. Res.*, *106*, 23,929–23,945, 2001.
- Soderblom, L. A., K. Edwards, E. M. Eliason, E. M. Sanchez, and M. P. Charette, Global color variations on the Martian surface, *Icarus*, *34*, 446–464, 1978.
- Thomas, P., Martian intracrater splotches: Occurrence, morphology, and colors, *Icarus*, *57*, 205–227, 1984.
- Thomas, P. C., et al., Bright dunes on Mars, *Nature*, *397*, 592–594, 1999.
- Thomson, J. L., and J. W. Salisbury, The mid-infrared reflectance of mineral mixtures (7–14 $\mu$ m), *Remote Sens. Environ.*, *43*, 1–13, 1993.
- Toon, O. B., J. B. Pollack, and C. Sagan, Physical properties of the particles composing the Martian dust storm of 1971–1972, *Icarus*, *30*, 663–696, 1977.
- Toulmin, P., A. K. Baird, B. C. Clark, K. Keil, H. J. Rose, R. P. Christian, P. H. Evans, and W. C. Kelliher, Geochemical and mineralogical interpretation of the Viking inorganic chemical results, *J. Geophys. Res.*, *82*, 4625–4634, 1977.
- Wyatt, M. B., V. E. Hamilton, H. Y. McSween Jr., P. R. Christensen, and L. A. Taylor, Analysis of terrestrial and Martian volcanic compositions using thermal emission spectroscopy, 1, Determination of mineralogy, chemistry, and classification strategies, *J. Geophys. Res.*, *106*, 14,711–14,732, 2001.
- Zuber, M. T., et al., Internal structure and early thermal evolution of Mars from Mars Global Surveyor topography and gravity, *Science*, *287*, 1788–1793, 2000.

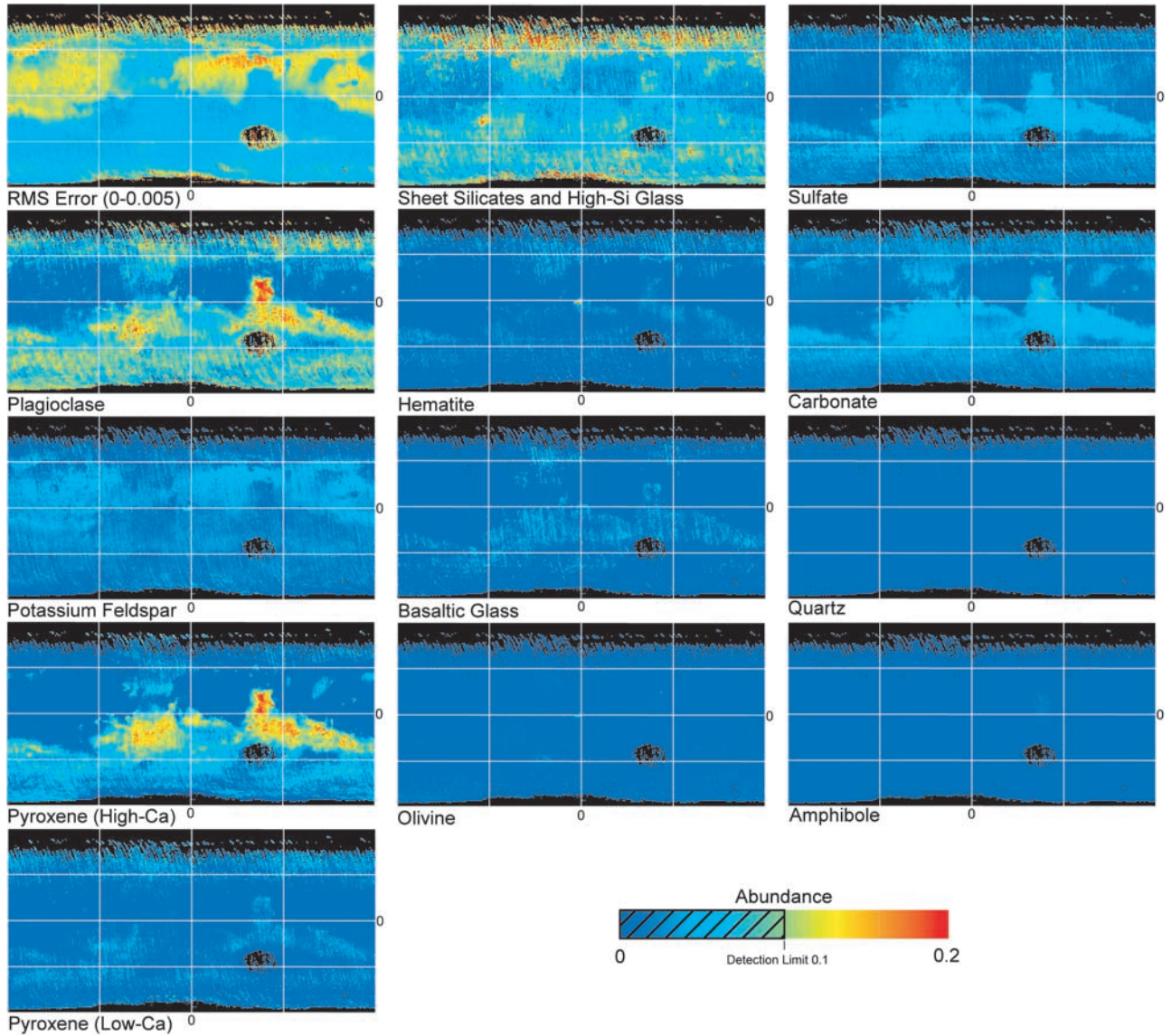


**Figure 2.** One pixel per degree binned global mineral concentration maps. The scale ranges from blue (concentration = 0) to red (concentration  $\geq 0.2$ ) except the RMS error image, which is 0 to 0.005 in emissivity from blue to red, respectively. Colors that are below the detection limit are hatched on the scale bar. The concentrations represent weightings relative to the mineral end-members used in the deconvolution (see text). Mineral groupings are described in the text and are listed in Table 1.